Washington University School of Medicine

Digital Commons@Becker

6-16-2023

Genetic deletion of skeletal muscle iPLA2γ results in mitochondrial dysfunction, muscle atrophy and alterations in whole-body energy metabolism

Sung Ho Moon
Washington University School of Medicine in St. Louis

Beverly Gibson Dilthey
Washington University School of Medicine in St. Louis

Shaoping Guan
Washington University School of Medicine in St. Louis

Harold F Sims
Washington University School of Medicine in St. Louis

Sara K Pittman
Washington University School of Medicine in St. Louis

See next page for additional authors

Follow this and additional works at: https://digitalcommons.wustl.edu/oa_4

Part of the Medicine and Health Sciences Commons

Please let us know how this document benefits you.

Recommended Citation

Authors

Sung Ho Moon, Beverly Gibson Dilthey, Shaoping Guan, Harold F Sims, Sara K Pittman, Amy L Keith, Christopher M Jenkins, Conrad C Weihl, and Richard W Gross

Article

Genetic deletion of skeletal muscle iPLA$_2$γ results in mitochondrial dysfunction, muscle atrophy and alterations in whole-body energy metabolism
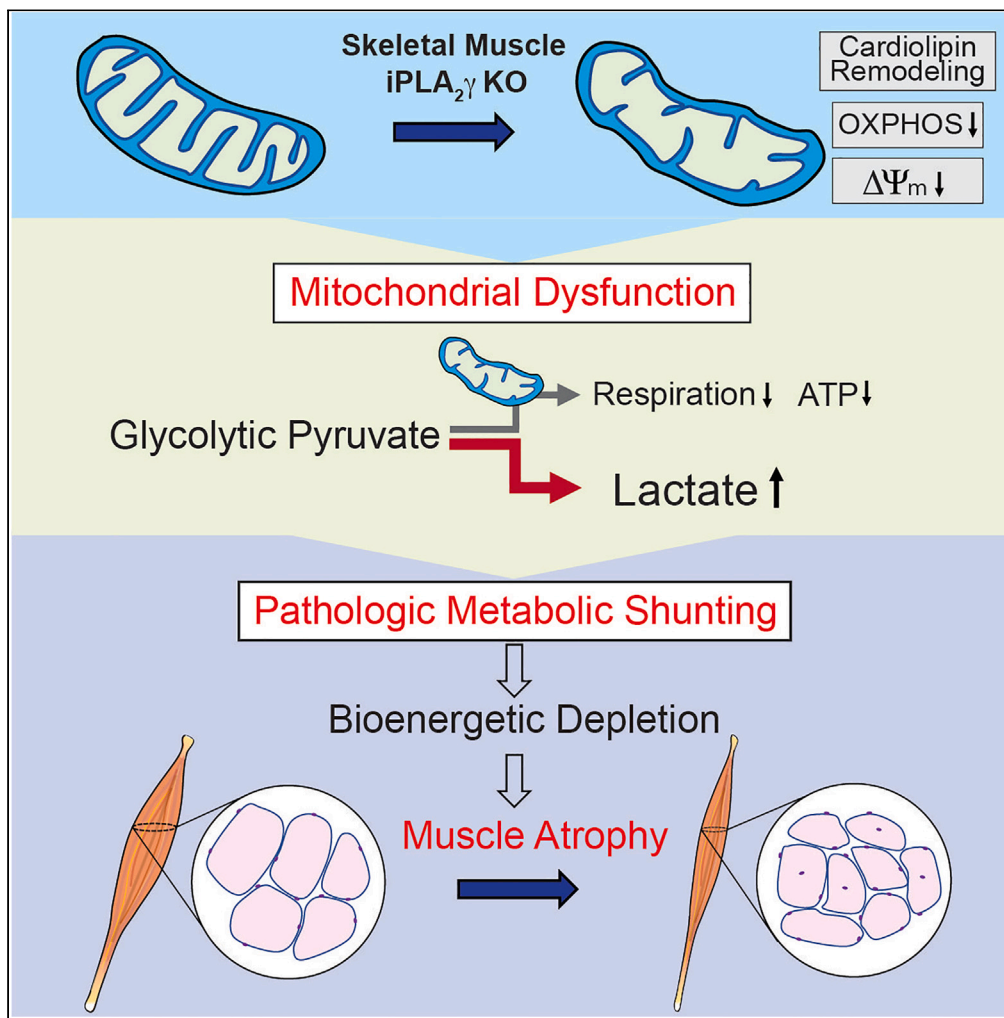
Sung Ho Moon, Beverly Gibson Dilthey, Shaoping Guan, ..., Christopher M. Jenkins, Conrad C. Weihl, Richard W. Gross

rgross@wustl.edu

Highlights
Skeletal muscle iPLA$_2$γ ablation induces progressive muscle weakness and atrophy

Genetic knockout of iPLA$_2$γ disrupts mitochondrial function and bioenergetics

Mitochondrial morphology and lipid homeostasis are disrupted by deletion of iPLA$_2$γ

Skeletal muscle iPLA$_2$γ contributes to regulation of whole-body energy metabolism

Article

Genetic deletion of skeletal muscle iPLA$_2\gamma$ results in mitochondrial dysfunction, muscle atrophy and alterations in whole-body energy metabolism

Sung Ho Moon,[1] Beverly Gibson Dilthey,[1] Shaoping Guan,[1] Harold F. Sims,[1] Sara K. Pittman,[2] Amy L. Keith,[2] Christopher M. Jenkins,[1] Conrad C. Weihl,[2] and Richard W. Gross[1,3,4,5,6,*]

SUMMARY

Skeletal muscle is the major site of glucose utilization in mammals integrating serum glucose clearance with mitochondrial respiration. To mechanistically elucidate the roles of iPLA$_2\gamma$ in skeletal muscle mitochondria, we generated a skeletal muscle-specific calcium-independent phospholipase A$_2\gamma$ knockout (SKMiPLA$_2\gamma$KO) mouse. Genetic ablation of skeletal muscle iPLA$_2\gamma$ resulted in pronounced muscle weakness, muscle atrophy, and increased blood lactate resulting from defects in mitochondrial function impairing metabolic processing of pyruvate and resultant bioenergetic inefficiency. Mitochondria from SKMiPLA$_2\gamma$KO mice were dysmorphic displaying marked changes in size, shape, and interfibrillar juxtaposition. Mitochondrial respirometry demonstrated a marked impairment in respiratory efficiency with decreases in the mass and function of oxidative phosphorylation complexes and cytochrome c. Further, a pronounced decrease in mitochondrial membrane potential and remodeling of cardiolipin molecular species were prominent. Collectively, these alterations prevented body weight gain during high-fat feeding through enhanced glucose disposal without efficient capture of chemical energy thereby altering whole-body bioenergetics.

INTRODUCTION

Skeletal muscle is the predominant tissue responsible for glucose uptake and utilization in mammals. Under physiologic conditions of metabolic demand, skeletal muscle metabolizes the majority of glucose resulting both from the predominance of glucose uptake into skeletal muscle, and the subsequent utilization of glycolytically derived pyruvate for mitochondrial oxidative phosphorylation. Accordingly, serum glucose clearance is largely regulated by insulin-stimulated skeletal muscle glucose uptake and its downstream glycolytic and mitochondrial metabolic end products, which modulate multiple inter-organ signaling networks and suites of downstream response elements.[1–3] This inter-organ communication plays a critical role in metabolic flexibility facilitating cellular adaptation to alterations in nutritional, metabolic, and muscle contractile performance.[4]

In industrialized societies over 90% of diabetes is due to insulin resistance which attenuates insulin-mediated glucose uptake and its downstream metabolism. Since insulin-resistance attenuates skeletal muscle glucose uptake from serum, this necessitates a metabolic switch from glucose metabolism to fatty acid utilization to compensate for decreased glucose-fueled energy production. Furthermore, recent studies have demonstrated that skeletal muscle can also secrete myokines that serve as paracrine, autocrine, and endocrine signaling molecules that communicate its metabolic and bioenergetic status enabling the efficient metabolic flexibility required for integrated organismal survival during stress.[5] Thus, skeletal muscle assumes a critical role in the production, regulation, and efficiency of energy production in response to external perturbations.

Phospholipases A$_2$ (PLA$_2$s) catalyze the hydrolysis of phospholipids resulting in the release of non-esterified fatty acids with the concomitant production of lysolipids. The subsequent oxidation of the cleaved lipids containing polyunsaturated acyl chains generates a variety of oxidized lipids that serve as mediators of

[1]Division of Bioorganic Chemistry and Molecular Pharmacology, Department of Medicine, Washington University School of Medicine, Saint Louis, MO 63110, USA

[2]Department of Neurology, Washington University School of Medicine, Saint Louis, MO 63110, USA

[3]Department of Developmental Biology, Washington University School of Medicine, Saint Louis, MO 63110, USA

[4]Center for Cardiovascular Research, Washington University School of Medicine, Saint Louis, MO 63110, USA

[5]Department of Chemistry, Washington University, Saint Louis, MO 63130, USA
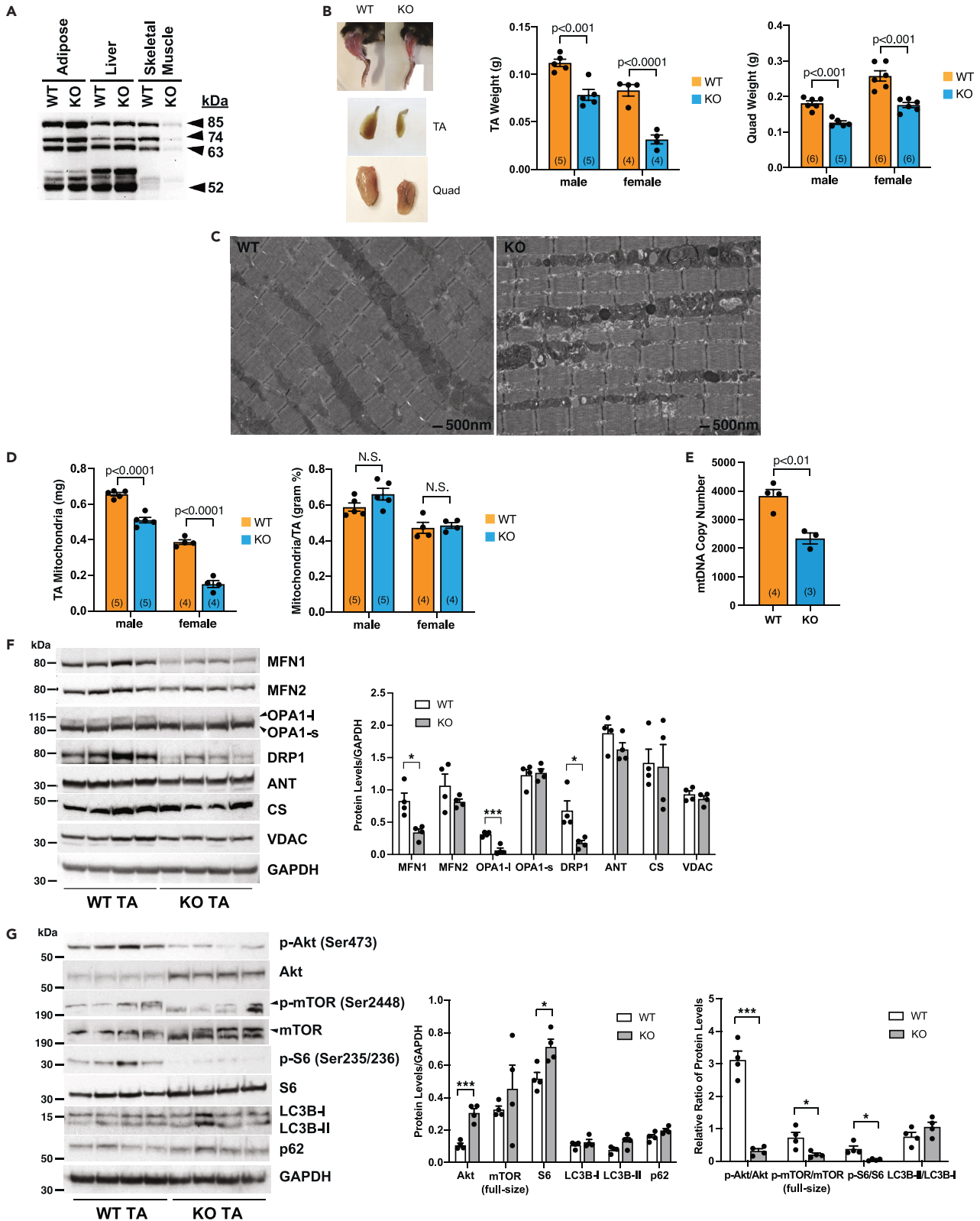
[6]Lead contact

*Correspondence: rgross@wustl.edu

https://doi.org/10.1016/j.isci.2023.106895

Figure 1. Skeletal muscle-specific deletion of iPLA$_2\gamma$ results in altered mitochondrial structure and impaired protein synthesis leading to skeletal muscle atrophy

(A) iPLA$_2\gamma$ protein levels in multiple tissues including white adipose tissue, liver, and skeletal muscle from WT and SKMiPLA$_2\gamma$KO mice were analyzed by western blot analysis indicating skeletal muscle-specific ablation of iPLA$_2\gamma$. The predominant isoforms of iPLA$_2\gamma$ (i.e., 85, 74, 63, and 52 kDa bands) in WT skeletal muscle are indicated by arrows.

(B) Tibialis anterior (TA) and quadriceps (Quad) muscles were excised from both legs of WT and SKMiPLA$_2\gamma$KO mice and weighed. The numbers of mice used for each sample set in the bar graphs are indicated in parentheses.

(C) Representative transmission electron microscopy (TEM) images of longitudinal sections of skeletal muscle TA fibers from WT and SKMiPLA$_2\gamma$KO mice (7 months old) demonstrating mitochondria with irregular cristae and electron dense inclusions present in the KO mouse resulting in disruption of normal striated muscle structure. See also Figure S1.

(D) Mitochondria were isolated from WT and SKMiPLA$_2\gamma$KO mice (7 months old) by differential centrifugation and the total yield of mitochondrial protein was determined by a BCA protein assay (left panel). The mitochondrial weight to tissue mass ratio was calculated for each indicated condition (right panel). Values from multiple independent preparations (indicated in parentheses in the bar graphs) are the average ± SEM. N.S., not significant.

(E) Copy number of mitochondrial DNA (ND1 gene) relative to nuclear DNA (HK2 gene) in TA from WT and SKMiPLA$_2\gamma$KO mice were determined using qPCR.

(F) Immunoblot analyses of mitochondrial proteins including MFN1, MFN2, OPA1-l (long form), OPA1-s (short form), DRP1, ANT, citrate synthase (CS), and VDAC from WT and SKMiPLA$_2\gamma$KO mouse TA muscle homogenates. See also Figure S2.

(G) Immunoblot analyses of proteins involved in protein synthesis and autophagy. *p < 0.05 and ***p < 0.001.

signal transduction that regulate a vast array of cellular functions.[6,7] A wide range of factors that alter insulin signaling in the diabetic state have been reported to be mediated by abnormal PLA$_2$-catalyzed lipid metabolism that can result in ROS generation and oxidative stress.[8–10] In previous work, we identified a mitochondrial membrane-associated phospholipase, iPLA$_2\gamma$ (also known as PNPLA8), whose germline ablation in mouse resulted in pathologic changes in mitochondrial ultrastructural morphology, respiratory function, metabolism, and membrane composition in all examined tissues.[10–13] Curiously, the global iPLA$_2\gamma$ knockout (KO) mouse displayed increased glucose clearance after glucose challenge and was resistant to body weight gain after high-fat feeding.[11] These findings were of particular interest as they suggested potential avenues to enhance glucose clearance, decrease the sequelae of diabetes, and attenuate diet-induced obesity. However, due to the deleterious effects of iPLA$_2\gamma$ loss of function on multiple organs in the germline iPLA$_2\gamma$ mouse, it was impossible to identify the tissue specific roles of iPLA$_2\gamma$ in skeletal muscle, the major tissue responsible for glucose clearance, in the observed salutary effects for glucose tolerance tests, and the prevention of obesity. Furthermore, the relevance of iPLA$_2\gamma$-mediated pathologies in humans was underscored by the discovery of a severely ill patient null for both iPLA$_2\gamma$ alleles that was identified through exome sequencing identifying a premature stop codon for iPLA$_2\gamma$ in both alleles.[14] This patient demonstrated marked mitochondrial morphologic alterations, muscle weakness, and lactic acidosis. A subsequent study reported two more unrelated patients with loss-of-function variants in PNPLA8 encoding iPLA$_2\gamma$ and similar pathologic alterations.[15] Accordingly, we hypothesized that skeletal muscle mitochondrial dysfunction precipitated by iPLA$_2\gamma$ loss of function resulted in deleterious changes in inter-organ communication in metabolic disease states, such as diet-induced obesity.

To specifically determine the mechanistic role of skeletal muscle iPLA$_2\gamma$ in glucose clearance, mitochondrial function, and organismal bioenergetics, we generated a skeletal muscle-specific iPLA$_2\gamma$ knockout (SKMiPLA$_2\gamma$KO) mouse by breeding floxed mice that possesses *loxP* sites flanking exon 5 of the iPLA$_2\gamma$ gene (which encodes the active site of iPLA$_2\gamma$) with a skeletal muscle-specific Cre recombinase transgenic mouse. Deletion of skeletal muscle iPLA$_2\gamma$ resulted in the disruption of muscle mitochondrial structural integrity, impaired mitochondrial respiration, decreased membrane potential, altered cardiolipin (CL) content/molecular species composition leading to inhibition of electron transport chain complexes that collectively resulted in severe lactic acidosis during physiologic stress. Moreover, the SKMiPLA$_2\gamma$KO mouse exhibited substantially altered whole-body energy storage and utilization in both liver and adipose tissue demonstrating its critical role in the integration of organismal bioenergetics.

RESULTS

Skeletal muscle-specific deletion of iPLA$_2\gamma$ results in altered mitochondrial structure and impaired protein synthesis leading to skeletal muscle atrophy

To discriminate between the functional consequences of iPLA$_2\gamma$ germline ablation and the specific effects of iPLA$_2\gamma$ KO in skeletal muscle, we generated a skeletal muscle-specific iPLA$_2\gamma$ knockout (SKMiPLA$_2\gamma$KO) mouse. Western blot analysis confirmed the tissue specific ablation of iPLA$_2\gamma$ (Figure 1). Previously, we demonstrated that the gene for iPLA$_2\gamma$ encodes for multiple different molecular weight isoforms
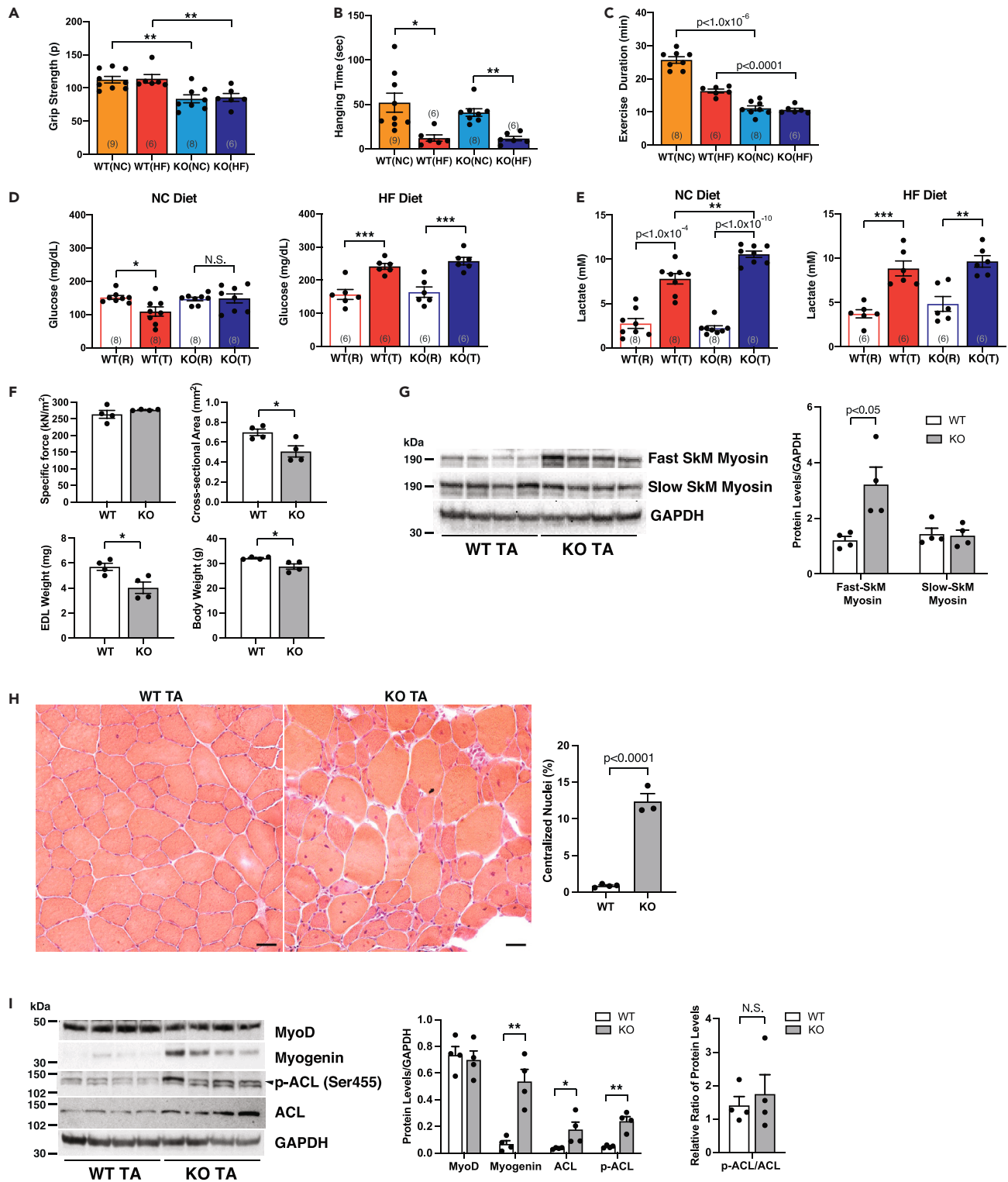
Figure 2. Skeletal muscle weakness with concomitant muscle fiber degeneration is present in SKMiPLA$_2$γKO mice

(A–C) A forearm grip test (A), four-limb hanging test (B), and treadmill exercise test (C) were performed with WT and SKMiPLA$_2$γKO male mice at 7–8 months of age. Grip force was measured as pond units (p = 0.00980665 N). See also Figure S3.

Figure 2. Continued

(D and E) Blood glucose (D) and lactate levels (E) in mice fed either a normal-chow (NC) or high-fat (HF) diet at rest (R) before and after treadmill exercise (T) were measured from blood samples taken from the tail vein. Values are expressed as the mean of multiple measurements from the indicated mice (mouse numbers indicated in the parenthesis in the bar graphs) $\pm$ SEM. *p < 0.05, **p < 0.01 and ***p < 0.001. N.S., not significant. See also Figure S3.

(F) Isometric maximal tetanic force measurements were performed on EDL muscles isolated from 4 WT and 4 SKMiPLA$_2\gamma$KO mice. The specific force after normalization to muscle cross-sectional area (PCSA) was determined. Individual values for PCSA, EDL muscle mass, and body weights of the mice that were utilized for force measurements are shown. *p < 0.05.

(G) Relative fiber type distribution present in the tibialis anterior (TA) muscle of WT and SKMiPLA$_2\gamma$KO mice are compared by immunoblot analysis for fast-skeletal and slow-skeletal myosin.

(H) Representative histological images of H & E staining of the TA muscles from WT and SKMiPLA$_2\gamma$KO are shown for comparison. TA from SKMiPLA$_2\gamma$KO mice displayed decreased muscle fiber size and an increased number of central nuclei. Scale bar: 50 μm. See also Figure S4.

(I) Immunoblot analyses of MyoD, Myogenin, ATP citrate lyase (ACL), and phospho-ACL (Ser455) from WT and SKMiPLA$_2\gamma$KO mouse TA muscle (n = 4). *p < 0.05 and **p < 0.01. N.S., not significant.

corresponding to 85, 74, 63, and 52 kDa that are present in distinct ratios in different tissues.[16,17] Importantly, the expression levels of the iPLA$_2\gamma$ isoforms in liver and white adipose tissue from the SKMiPLA$_2\gamma$KO mouse were unchanged in comparison to those present in WT mice (Figure 1A). In contrast, mitochondrial iPLA$_2\gamma$ protein expression levels in skeletal muscle tissues were nearly completely ablated in SKMiPLA$_2\gamma$KO mice. The data also demonstrate that the lower molecular weight isoforms of iPLA$_2\gamma$ (< 63 kDa) were absent or markedly reduced in wild-type skeletal muscle.

A prominent physical difference of the SKMiPLA$_2\gamma$KO mouse in comparison to WT controls was the decrease in the size/weight of the tibialis anterior (TA) and quadriceps (Quad) muscle groups that were decreased by 30% in male mice (Figure 1B). Examination of gender differences demonstrated a greater loss of TA mass in females in comparison to males by deletion of iPLA$_2\gamma$. Next, we examined the microscopic ultrastructure of the TA muscle of the SKMiPLA$_2\gamma$KO mouse by transmission electron microscopy (TEM). TEM image analysis of the TA muscle from WT and KO mice demonstrated a prevalence of mitochondria with severe ultrastructural damage, including irregular cristae and electron dense inclusions present in the KO mouse accompanied by the disruption of normal striated muscle structure (Figures 1C and S1). However, the mass ratio of total recoverable mitochondria isolated by differential centrifugation to total TA mass was not significantly different between WT and SKMiPLA$_2\gamma$KO, regardless of gender (Figure 1D). This result was supported by western blot analyses showing no significant differences in normalized expression levels of abundant mitochondrial marker proteins including VDAC, ANT, and citrate synthase (CS) from WT and iPLA$_2\gamma$ KO TA muscle tissue (Figure 1F). In contrast, mtDNA copy number in SKMiPLA$_2\gamma$KO TA muscle was significantly decreased indicating alterations in mitochondrial content due to disrupted -mtDNA maintenance processes (Figure 1E). Furthermore, despite only modest decreases in mRNA levels of DRP1, OPA1, and MFN1 relative to WT controls, the expression levels of these proteins were dramatically diminished in SKMiPLA$_2\gamma$KO TA muscle, which likely contributed to the observed decrease in mtDNA copy number and the altered morphology of the mitochondria (Figures 1F and S2).

To investigate possible mechanisms for the observed muscle atrophy in SKMiPLA$_2\gamma$KO mice, we examined alterations in protein markers of altered protein synthesis and autophagy. The results indicated that protein synthesis via the Akt/mTOR muscle growth pathway involving S6 ribosomal protein activation was significantly impaired due to dramatic decreases in phosphorylation (indicating activation) of these proteins despite compensatory upregulation of Akt and S6 protein mass (Figure 1G). Interestingly, cleavage of mTOR was prominent in SKMiPLA$_2\gamma$KO mouse muscle as shown in western blots as a lower molecular weight isoform indicative of an inhibition of mTOR activity. Autophagocytic flux monitored by LC3B-I/II and p62 (p62/SQSTM1) protein expression levels was not significantly changed in SKMiPLA$_2\gamma$KO mouse TA muscle when compared with WT controls (Figure 1G). Thus, reduction of the net rate of protein synthesis in the presence of bioenergetic inefficiency likely underlies the skeletal muscle atrophy present in the SKMiPLA$_2\gamma$KO mouse.

Skeletal muscle weakness with concomitant muscle fiber degeneration is present in SKMiPLA$_2\gamma$ KO mice

Since mitochondrial and microscopic muscular structures were significantly altered in the SKMiPLA$_2\gamma$KO mouse, we next evaluated muscular motor function in these mice in comparison to WT littermates fed either a normal-chow (NC) or high-fat (HF) diet (Figure 2). Both grip tests and treadmill exercise tests
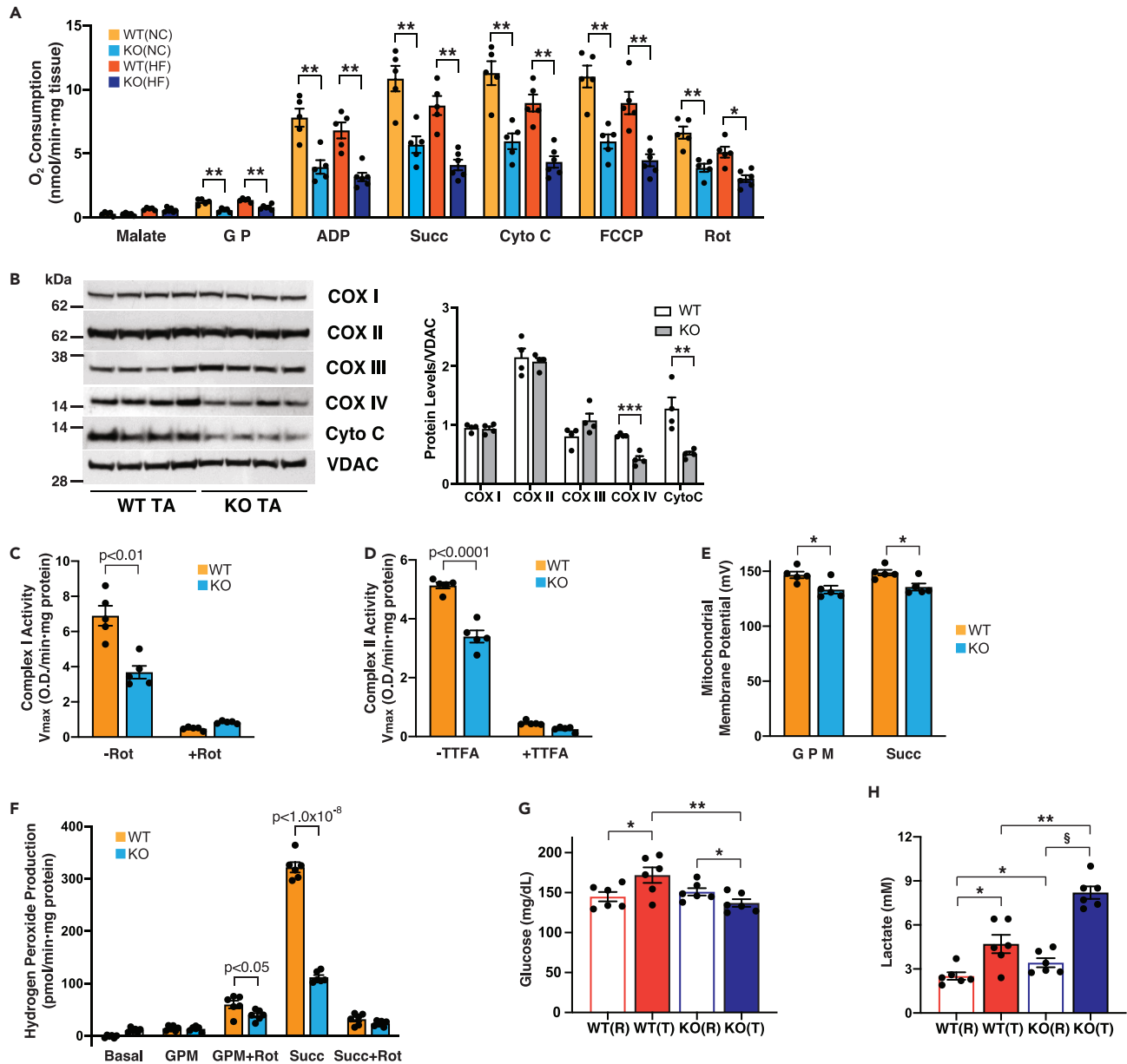
Figure 3. Mitochondrial respiration in SKMiPLA$_2\gamma$KO skeletal muscle is significantly attenuated with dramatic decreases in the activities and expression levels of electron transfer chain complexes

(A) High-resolution mitochondrial respirometry was performed by utilizing permeabilized tibialis anterior (TA) muscle tissue. 5 WT and 5 KO mice fed an NC diet, and 5 WT and 6 KO mice fed an HF diet were utilized for independent measurements. *p < 0.05 and **p < 0.01. See also Figure S5.

(B) Protein expression levels of respiratory electron chain complexes including Complex I ∼ IV and cytochrome *c* in WT vs. SKMiPLA$_2\gamma$KO TA were determined by western blot analyses. **p < 0.01 and ***p < 0.001.

(C and D) Complex I and II catalytic activities were assayed by using membrane-disrupted mitochondria isolated from TA muscle of 5 WT and 5 SKMiPLA$_2\gamma$KO mice fed an NC diet, in the presence of substrates (*i.e.*, NADH and succinate, respectively) with decylubiquinone and DCIP as a terminal electron acceptor. Complex I and II activities were confirmed by using their specific inhibitors, rotenone (Rot) and TTFA, respectively. Values are expressed as means ± SEM.

(E) Membrane potential of mitochondria isolated from TA muscle was measured by using a TPP·Cl electrode. Independent measurements with 5 WT and 5 KO mice were utilized. Glutamate/pyruvate/malate (G P M) or succinate (Succ) were used as substrates for mitochondrial membrane potentiometry. *p < 0.05.

Figure 3. _Continued_

(F) Mitochondria isolated from TA muscle of 6 WT and 6 KO mice were placed in respiration buffer. Mitochondria were incubated with either glutamate/pyruvate/malate (G P M) or succinate (Succ) substrate in the presence or absence of 1 μM rotenone (Rot). The amount of H_2O_2 in the buffer (indicative of superoxide production) was determined by Amplex Red.

(G and H) Glucose (G) and lactate levels (H) in blood from 6 WT to 6 SKMiPLA$_2$γKO female mice before (R) and after (T) intense treadmill exercise at a speed of 18 m/min for 4 min were measured. Note that 3 out of 6 KO mice were completely exhausted within 1–2.5 min and their glucose and lactate levels were measured immediately upon reaching exhaustion. $*p < 0.05$, $**p < 0.01$ and $\S p < 1.0 \times 10^{-7}$.

revealed that the iPLA$_2$γ KO mouse had a weaker grip force and was more rapidly fatigued during treadmill exercise. These results indicate that deletion of skeletal muscle iPLA$_2$γ resulted in compromised skeletal muscle mechanical function. These differences were not significantly altered with either diet type or gender (Figures 2A–2C and S3). Next, blood glucose and lactate levels before and after treadmill exercise were monitored. Although blood glucose levels of WT mice fed an NC-diet mildly decreased while exercising to exhaustion, similarly measured blood glucose levels of SKMiPLA$_2$γKO mice exercised to exhaustion were unchanged due to the shorter duration of treadmill exercise (Figure 2D). Conversely, serum lactate levels present in the SKMiPLA$_2$γKO mouse after exercise on the treadmill increased more than WT despite a shorter average exercise duration time (Figure 2E). Blood glucose and lactate levels after exercise were increased in both WT and KO mice fed an HF diet relative to their corresponding NC diet controls, regardless of exercise duration. To further investigate the physiologic impact of iPLA$_2$γ loss of function on contractile muscle function, _ex vivo_ isometric maximum muscle force measurements using EDL muscle were performed. EDL muscle weight as well as the total body weight of the SKMiPLA$_2$γKO mouse were lower than WT controls resulting in a smaller physiological cross-sectional area (PCSA). Muscle force measurements indicated that specific tetanic peak tensions after normalization to PCSA were not different between WT and SKMiPLA$_2$γKO mice (Figure 2F). Interestingly, fast-twitch TA muscle from the SKMiPLA$_2$γKO mouse was further shifted toward a fast-twitch type II muscle fiber phenotype as determined by western blot analysis for fast- and slow-skeletal muscle myosin (Figure 2G).

Next, we examined the histology of muscle fibers from WT and SKMiPLA$_2$γKO mice using hematoxylin & eosin (H & E) staining. TA muscle cross sections from the SKMiPLA$_2$γKO mouse displayed internalization of nuclei and a smaller apparent myocyte diameter while those from WT had a relatively larger diameter and multiple peripheral nuclei (Figure 2H). Similarly, the Quad muscle in the SKMiPLA$_2$γKO mouse displayed irregularly sized myocytes with an increase in the number of markedly smaller myofibers (myofibrils) with normal peripheral nuclei (Figure S4). Although expression levels of the myogenic regulatory factor MyoD were essentially unchanged in the SKMiPLA$_2$γKO in comparison to WT controls, markedly increased expression of Myogenin due to iPLA$_2$γ loss of function in skeletal muscle is indicative of more active regenerative myogenesis in SKMiPLA$_2$γKO vs. WT mice (Figure 2I). Furthermore, the expression level of ATP citrate lyase (ACL), a key enzyme regulating muscle cell growth/differentiation, muscle type transition, and mitochondrial function,[18,19] and its active (phosphorylated at Ser455) form were moderately upregulated in SKMiPLA$_2$γKO mouse TA muscle likely facilitating skeletal muscle regeneration and the observed increase in fast skeletal myosin expression (Figure 2I).

Taken together, these results suggest that skeletal muscle glycolytic activity in the SKMiPLA$_2$γKO mouse is not likely compromised due to the accumulation of lactate after exercise and an unaltered maximum muscle force normalized to PCSA. However, these results also suggest that chronic mitochondrial dysfunction is present in the SKMiPLA$_2$γKO, which is accompanied by higher lactate levels and chronic cycles of muscle degeneration/regeneration, which are largely ineffective in restoring skeletal muscle mechanical function especially during metabolic or mechanical stress.

Mitochondrial respiration in SKMiPLA$_2$γKO skeletal muscle is significantly attenuated with dramatic decreases in the activities and expression levels of electron transfer chain complexes

Based on the aforementioned results, we hypothesized that skeletal muscle mitochondria from the SKMiPLA$_2$γKO are functionally compromised. To examine mitochondrial bioenergetics, we used high-resolution respirometry of permeabilized TA muscle from either WT or SKMiPLA$_2$γKO mice fed either an NC or HF diet. Saponin-permeabilized TA muscle was placed in buffer with high levels of dissolved oxygen (~400 μM) followed by addition of glutamate/pyruvate/malate to investigate the ability of mitochondria to utilize these anaplerotic/glycolytic/TCA cycle metabolites. Consistent with the above results, TA mitochondria isolated from SKMiPLA$_2$γKO male mice on an NC-diet consumed 50% less oxygen than
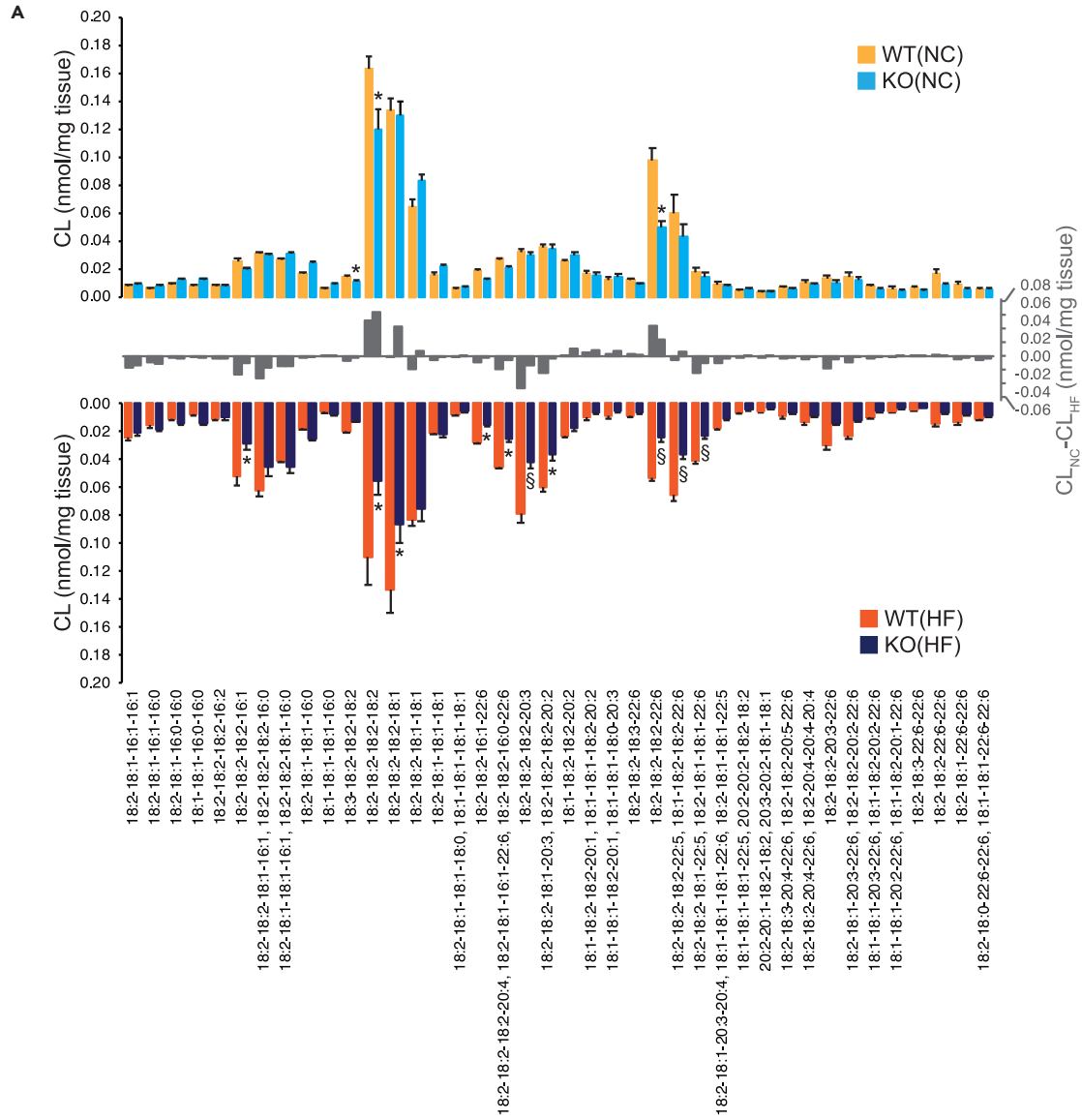
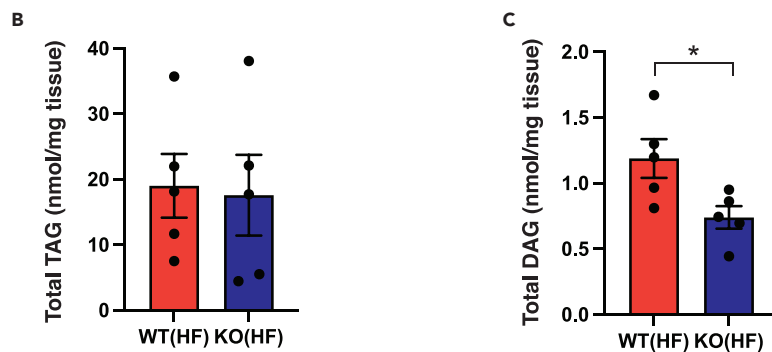Molecular Species of CL in Mouse Tibialis Anterior

Figure 4. Genetic ablation of iPLA$_2\gamma$ alters mitochondrial membrane cardiolipin content

Male mice (WT and SKMiPLA$_2\gamma$KO) were fed either a normal-chow (NC) or high-fat (HF) diet for 3 months starting at 3 months of age.

(A) Lipids from TA muscle were extracted and cardiolipin (CL) molecular species were identified. CL molecular species were quantified using tetra 14:0-CL as an internal standard (I.S.) through comparing peak intensities in the negative ion mode using the $[M-2H+1]^{2-}$ isotopologue peak of CL. 6 WT fed an NC diet, 5 WT fed an HF diet, 6 SKMiPLA$_2\gamma$KO fed an NC diet, and 5 SKMiPLA$_2\gamma$KO fed an HF diet were utilized. A mirror plot of CL molecular species with indicated acyl chain compositions from WT and KO mice fed an NC diet (top panel) or HF diet (lower panel) are presented with calculated differences (CL$_{NC}$-CL$_{HF}$) displayed between the two panels. Values are the means ± SEM. *p < 0.05 and §p < 0.005.

(B and C) Total contents of TAG (B) and DAG (C) in TA tissues from 5 WT to 5 SKMiPLA$_2\gamma$KO mice fed HF diet were determined. *p < 0.05.

WT controls under same conditions (Figure 3A). This difference was larger in WT vs. SKMiPLA$_2\gamma$KO female TA mitochondria, which is consistent with data showing greater decreases in muscle mass and mitochondria mass for female SKMiPLA$_2\gamma$KO mice relative to WT controls (Figure S5). For comparison, an HF diet mildly reduced oxygen consumption in both WT and KO mice without significantly changing the magnitude of the observed differences (Figure 3A).

To further investigate the mechanisms underlying the decrease in mitochondrial respiration present in TA skeletal muscle tissue from the SKMiPLA$_2\gamma$KO, we examined the effect of iPLA$_2\gamma$ ablation on protein expression levels of mitochondrial respiratory complexes by immunoblot analysis. Interestingly, the protein expression levels of complex IV and cytochrome c in SKMiPLA$_2\gamma$KO skeletal muscle were dramatically reduced in comparison to WT littermates (Figure 3B). Moreover, although the expression levels of complexes I and II were not detectably altered in KO TA muscle, the individually measured activities of complexes I and II were decreased by ∼ 50% and ∼ 25%, respectively, when compared with WT controls (Figures 3C and 3D). Next, the membrane potential of the inner mitochondrial membrane in isolated mitochondria from TA muscle of WT and SKMiPLA$_2\gamma$KO mice was determined by measuring extramitochondrial tetraphenylphosphonium chloride (TPP·Cl) levels in the presence of glutamate/pyruvate/malate or succinate as substrates. The mitochondrial membrane potential in SKMiPLA$_2\gamma$KO mouse TA muscle with complex I or complex II substrates (*i.e.*, glutamate/pyruvate/malate or succinate, respectively) was significantly lower than that of WT littermates (Figure 3E). Consistent with the lower membrane potential of SKMiPLA$_2\gamma$KO mitochondria, hydrogen peroxide production indicative of ROS generated from forward (*i.e.*, observed with glutamate/pyruvate/malate with rotenone) and reverse (*i.e.*, observed with succinate) electron transfer was greatly attenuated in SKMiPLA$_2\gamma$KO mice in comparison with WT controls (Figure 3F).

Next, we compared glucose consumption and lactate accumulation in WT vs. SKMiPLA$_2\gamma$KO mice after high-intensity short-duration treadmill training due to the diminished ability of skeletal muscle tissue from the KO mouse to utilize pyruvate for mitochondrial respiration resulting in premature exercise fatigue. For this purpose, mice were forced to run on treadmill at 18 m/min for 4 min after which blood glucose and lactate levels were measured. Consistent with the respiration results with isolated mitochondria, lactate accumulation in the blood of the SKMiPLA$_2\gamma$KO mouse markedly increased with a corresponding decline in blood glucose following intense exercise in comparisons with their WT counterparts (Figures 3G and 3H).

Collectively, these results indicate that deletion of skeletal muscle iPLA$_2\gamma$ affects the collective macroscopic properties of skeletal muscle including size, weight, and exercise performance, which results from defects in mitochondrial bioenergetics.

Ablation of iPLA$_2\gamma$ alters the cardiolipin content and bioenergetics of SKMiPLA$_2\gamma$KO skeletal muscle mitochondria

Cardiolipin (CL) is predominantly located in the inner mitochondrial membrane where it facilitates the formation and function of mitochondrial electron transfer chain supercomplexes.[20–22] Accordingly, we measured the levels of different CL molecular species using multidimensional mass spectrometry-based shotgun lipidomics. (Figure 4A). The results indicated that SKMiPLA$_2\gamma$KO TA muscle possessed significantly lower levels of tetra 18:2 CL, the most abundant mature form of CL molecular species in skeletal muscle, as well as decreased 22:6-containing CL molecular species during NC feeding. Interestingly, WT mice fed an HF diet exhibited decreased tetra-18:2 CL and increased 22-carbon long-chain polyunsaturated fatty acyl-containing CL in TA muscle which likely contributed to the HF diet-induced attenuation of mitochondrial respiration. In SKMiPLA$_2\gamma$KO mice fed an HF diet, CL showed a further decrease in 18:2 fatty acyl-containing CL in comparison to WT mice, although without a dramatic increase in 22-carbon-polyunsaturated fatty acyl-containing CL species. The level of DAG, but not TAG, in KO muscle tissue was
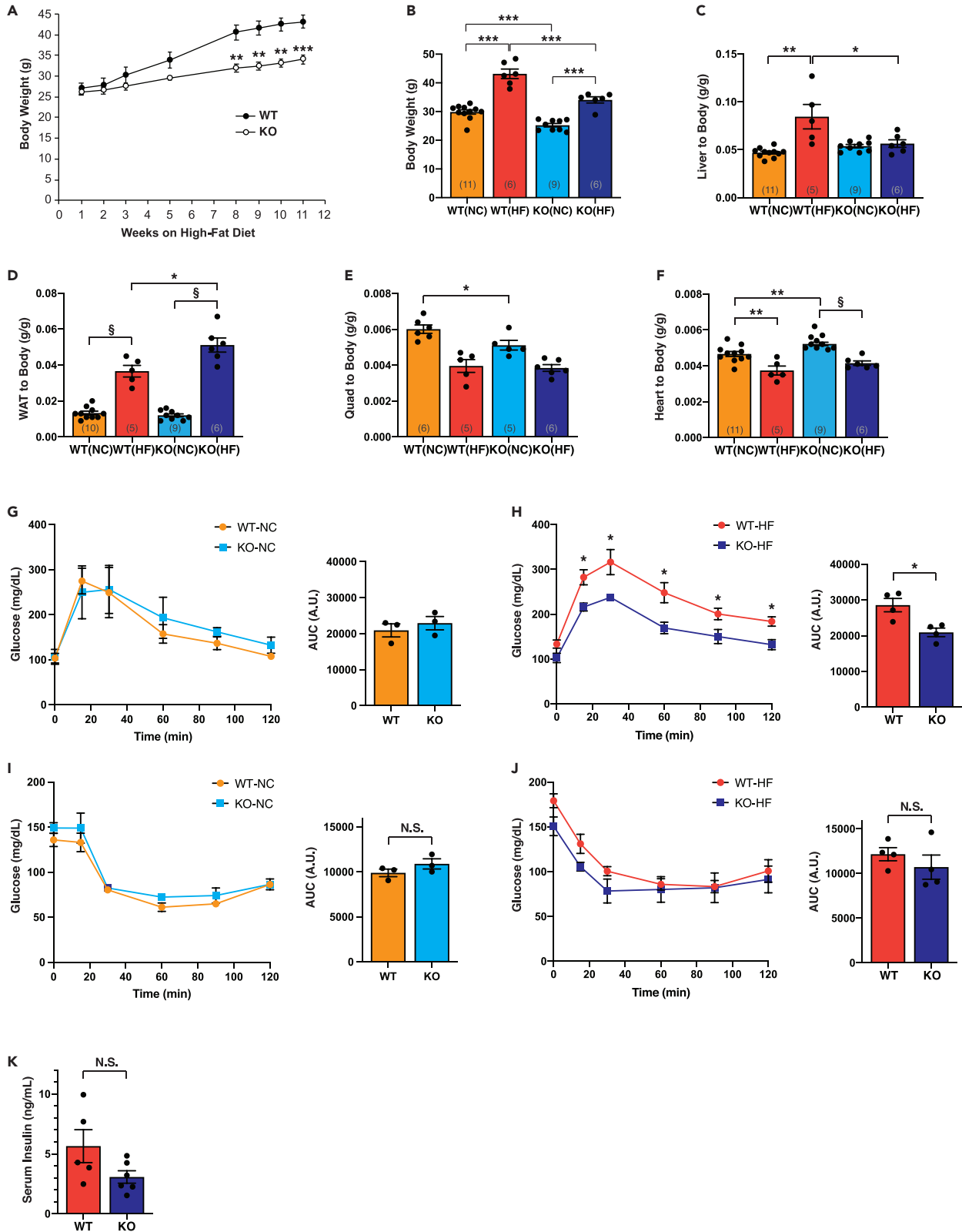
Figure 5. Deletion of skeletal muscle iPLA₂γ results in improved glucose tolerance and the inability to gain weight during high-fat feeding

Genetic ablation of skeletal muscle iPLA₂γ improves glucose tolerance and reduces weight gain during HF feeding.

(A) Body weights of 6 WT and 6 SKMiPLA₂γKO male mice fed an HF diet were monitored over 11 weeks following initiation of HF feeding at 3 months of age.

(B) Comparison of body weights of WT and SKMiPLA₂γKO mice at the end of 11 weeks (3 months) of NC or HF feeding.

(C–F) Tissue weights of liver (C), epididymal white adipose tissue (WAT) (D), quadriceps (Quad) (E), and heart (F) normalized to body weight were compared between WT and SKMiPLA₂γKO mice. Mouse numbers are indicated in the parenthesis in the bar graphs.

(G–J) glucose tolerance test (G and H) and insulin tolerance tests (I and J) for WT and SKMiPLA₂γKO mice either on a normal-chow (NC) diet or a high-fat (HF) diet were performed. AUC, area under the curve in arbitrary units (A.U.).

(K) Blood insulin levels from 5 WT to 6 SKMiPLA₂γKO mice after HF feeding were determined by ELISA analysis. *p < 0.05, **p < 0.01, ***p < 0.001 and §p < 0.0001.

significantly lower than WT (Figures 4B and 4C). These data suggest that loss of tetra-18:2 CL contributes to inefficient respiration through disruption of the stability and/or the association of ETC proteins likely resulting from alterations in mitochondrial membrane surface charge and molecular dynamics.

Deletion of skeletal muscle iPLA₂γ results in improved glucose clearance and the inability to gain weight during high-fat feeding

Since skeletal muscle consumes the majority of circulating blood glucose, it is tightly coupled with integrated organismal bioenergetics, including fatty acid utilization and the accumulation of triglycerides. Accordingly, we next examined the effects of skeletal muscle iPLA₂γ knockout and its resultant impact on whole-body energy metabolism after NC or HF feeding. First, we found that HF diet-induced weight gain present in WT mice was dramatically reduced in SKMiPLA₂γKO mice. Specifically, the net body mass increase of the SKMiPLA₂γKO mouse following consumption of an HF diet was on average ∼ 8g while WT mice gained ∼ 16g after 3-month of HF feeding (Figures 5A and 5B). Secondly, the weight ratio of wild-type mouse liver to body mass following HF feeding was increased by 80% when compared with NC-fed WT mouse liver. In stark contrast, the weight ratio of liver from SKMiPLA₂γKO mice fed an HF diet to body weight did not significantly differ from those of either NC-fed WT or NC-fed KO mice (Figure 5C). Interestingly, HF diet-induced increases in white adipose tissue mass were significantly more prominent in SKMiPLA₂γKO mice than WT controls (Figure 5D). Since the dysfunctional mitochondria in SKMiPLA₂γKO skeletal muscle cannot readily utilize serum fatty acids that are abundant during high-fat feeding, adipose tissue would be predicted to be a primary site of storage for the excess fatty acids in the KO mouse. Notably, no significant differences were observed in the ratios of either Quad/total body weight or heart/total body weight between WT and SKMiPLA₂γKO mice after HF feeding (Figures 5E and 5F).

Next, we examined serum glucose clearance in SKMiPLA₂γKO mice in comparisons to WT controls. Glucose tolerance (GTT) and insulin tolerance tests (ITT) for WT vs. SKMiPLA₂γKO mice fed a normal-chow diet did not reveal significant differences between the two strains (Figures 5G and 5I). However, genetic ablation of iPLA₂γ significantly improved the poor glucose clearance and insulin insensitivity in WT mice fed an HF-diet. For example, HF feeding of WT mice for 3 months resulted in markedly elevated blood glucose levels (∼ 320 mg/dL) at 30 min after glucose challenge (bolus i.p. injection) followed by gradual clearance of circulating glucose (Figure 5H). In contrast, SKMiPLA₂γKO mice displayed an improved response to glucose challenge resulting in a peak concentration of ∼ 240 mg glucose/dl and the decreased area under the curve during glucose challenge (Figure 5H). Although the SKMiPLA₂γKO mice exhibited a lower basal blood glucose level after HF feeding than wild-type controls, no significant differences in insulin tolerance and serum insulin levels in WT vs. KO were observed (Figures 5J and 5K). Collectively, the increased glucose clearance rate of the SKMiPLA₂γKO mouse fed an HF diet is likely indicative of increased glucose uptake and utilization by skeletal muscle myocytes for glycolysis, which leads to the accumulation of lactate due to the inability of the compromised SKMiPLA₂γKO mitochondria to process glycolytically derived pyruvate.

Attenuation of the pathologic accumulation of neutral lipids in the liver of the SKMiPLA₂γKO mouse following high-fat feeding

Since a high-fat diet did not induce increase the SKMiPLA₂γKO liver to body weight ratio, we examined hepatic tissue from both strains of mice for fat content. First, utilizing H & E staining and imaging, we found that the content of lipid droplets present in the HF-fed SKMiPLA₂γKO liver was dramatically less than HF-fed WT controls (Figure 6A). Secondly, the majority of TAG molecular species that accumulated in HF-fed WT liver were significantly lower in SKMiPLA₂γKO liver (Figures 6B, 6C, and S6A). Similarly, most DAG
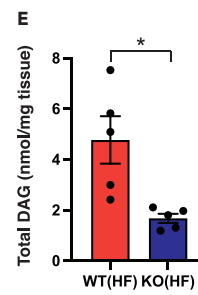
A

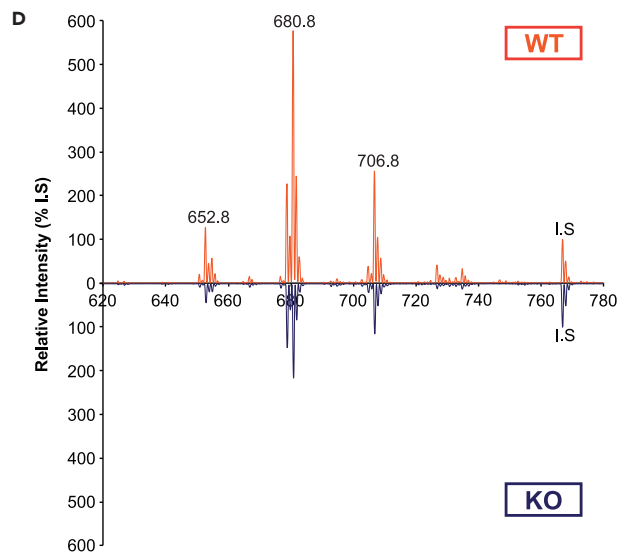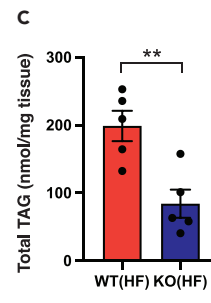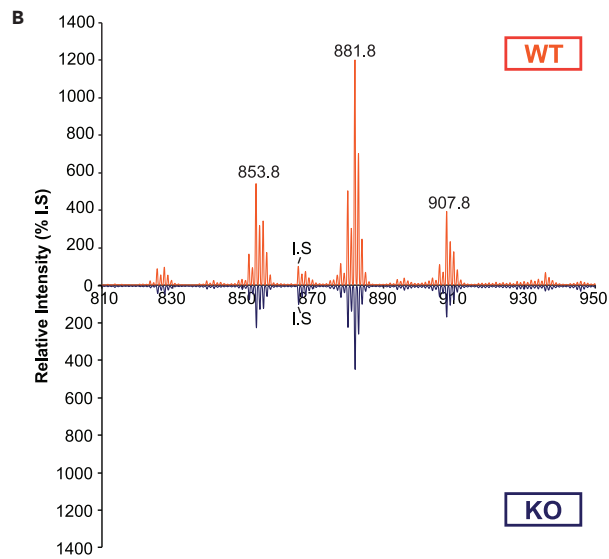WT   KO
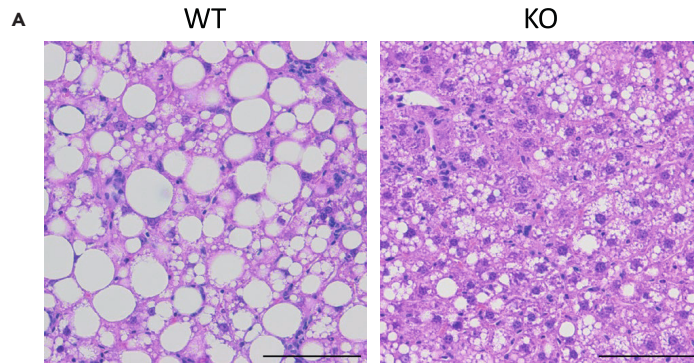

B

C

D

E

Figure 6. Pathologic accumulation of neutral lipids is attenuated in the liver of the SKMiPLA$_2\gamma$KO mouse following high-fat feeding

Skeletal muscle specific knockout of iPLA$_2\gamma$ alters energy metabolism preventing accumulation of neutral lipids in liver during HF feeding.

(A) Hepatic steatosis was evaluated by histological microscopic imaging. H & E staining was performed with liver sections obtained from WT and SKMiPLA$_2\gamma$KO mice after HF feeding. Fat droplets appear as vacuoles in the images. Scale bar: 100 μm.

(B–E) Triglyceride (B-C) and diglyceride (D-E) molecular species and amounts in WT (upper spectrum) and SKMiPLA$_2\gamma$KO (lower spectrum) hepatic tissue following HF feeding were determined by shotgun lipidomics utilizing mass spectrometry. Triacylglycerol (TAG) and diacylglycerol (DAG) levels were markedly increased in the livers of WT (n = 5) mice after HF feeding relative to SKMiPLA$_2\gamma$KO (n = 5) mice. Peak heights are normalized to tri-17:1-TAG and di-20:0-DAG internal standards (I.S.). *p < 0.05 and **p < 0.01. See also Figure S6.

molecular species that accumulated in HF-fed WT liver were also significantly lower in SKMiPLA$_2\gamma$KO liver (Figures 6D, 6E, and S6B). These results indicate that these differences in neutral lipid content likely contribute to the decreased mass of the liver in the SKMiPLA$_2\gamma$KO mice after HF feeding.

Next, we examined the glycogen content of WT and SKMiPLA$_2\gamma$KO liver by periodic acid-Shiff (PAS) staining and imaging. Hepatic tissue sections from WT and SKMiPLA$_2\gamma$KO mice fed an NC diet were treated with PAS stain and imaged for microscopic glycogen distribution within the tissue samples. Higher amounts of glycogen were present in iPLA$_2\gamma$ KO liver in comparison to WT liver controls (Figure 7A). The pronounced accumulation of glycogen in KO liver implies that glucose and pyruvate are inadequately utilized by iPLA$_2\gamma$ KO skeletal muscle and, at least in part, ultimately stored as glycogen in the liver. During HF feeding, ingestion of large amounts of lipids causes overexpression of IRS-1, GAPDH and GSK 3α/3β, and increased insulin secretion resulting in extensive steady state phosphorylation of GSK in WT liver (Figure 7B). However, these effects were absent or attenuated in SKMiPLA$_2\gamma$KO liver following HF feeding when compared with KO mice fed an NC diet. This result implies that KO mice challenged with an HF diet can adapt by increasing glucose uptake from the circulation. However, mitochondrial bioenergetic inefficiency limits the amount of chemical energy that can be extracted from glucose leading to the accumulation of lactate in skeletal muscle. Further, we propose that the liver attempts to compensate for the bioenergetic inefficiency resulting from skeletal muscle mitochondrial dysfunction by utilization of endogenous lipid substrates. Subsequent depletion of hepatic lipid stores in the SKMiPLA$_2\gamma$KO result in low serum lipid concentrations, which prevent the induction of insulin resistance that typically results from HF feeding. Furthermore, decreased hepatic steatosis in SKMiPLA$_2\gamma$KO mice fed an HF diet in comparisons with WT controls resulted in a diminished incidence of HF diet-induced fibrosis (Figure 7C). Taken together, these results indicate that SKMiPLA$_2\gamma$KO mice effectively catabolize hepatic neutral lipids during HF feeding in order to compensate for the altered utilization/storage of glucose in liver arising from the impairment of skeletal muscle mitochondrial respiration due to iPLA$_2\gamma$ loss of function.

DISCUSSION

Skeletal muscle plays a predominant role in regulating whole-body glucose uptake and metabolism in vertebrate animals. Numerous previous studies in mice and other mammals have demonstrated that abnormalities in skeletal muscle glucose utilization affect whole-body energy metabolism and insulin sensitivity.[23,24] Thus, the ability of skeletal muscle to extract circulating glucose and efficiently metabolize it to generate chemical energy (*i.e.*, ATP) is a principal determinant of mammalian bioenergetics. Failure of either the cellular uptake of glucose or its efficient conversion to chemical energy is an underlying theme in multiple disease states with a wide variety of downstream pathologic sequelae.[25] The generation and characterization of the SKMiPLA$_2\gamma$KO mouse demonstrate the prominent role of iPLA$_2\gamma$ in the physiologic function of skeletal muscle mitochondria in the context of the whole animal. Salient features of mitochondrial alterations in the SKMiPLA$_2\gamma$KO mouse include specific changes in the skeletal muscle mitochondrial lipid composition, morphology and respiratory efficiency. Further, these dysfunctional changes result in increased turnover of individual skeletal muscle myocytes demonstrated by the abundance of centralized nuclei indicative of newly formed myocytes that replace/replenish dysfunctional myocytes in skeletal muscle.

Knock-out of iPLA$_2\gamma$ displays tissue-specific phenotypic changes in glucose/lipid metabolism and bioenergetics during metabolic stress

Previous studies have demonstrated that activation of phospholipases can result in protean alterations in intracellular lipid composition and metabolism in a wide range of disease states including diet-induced
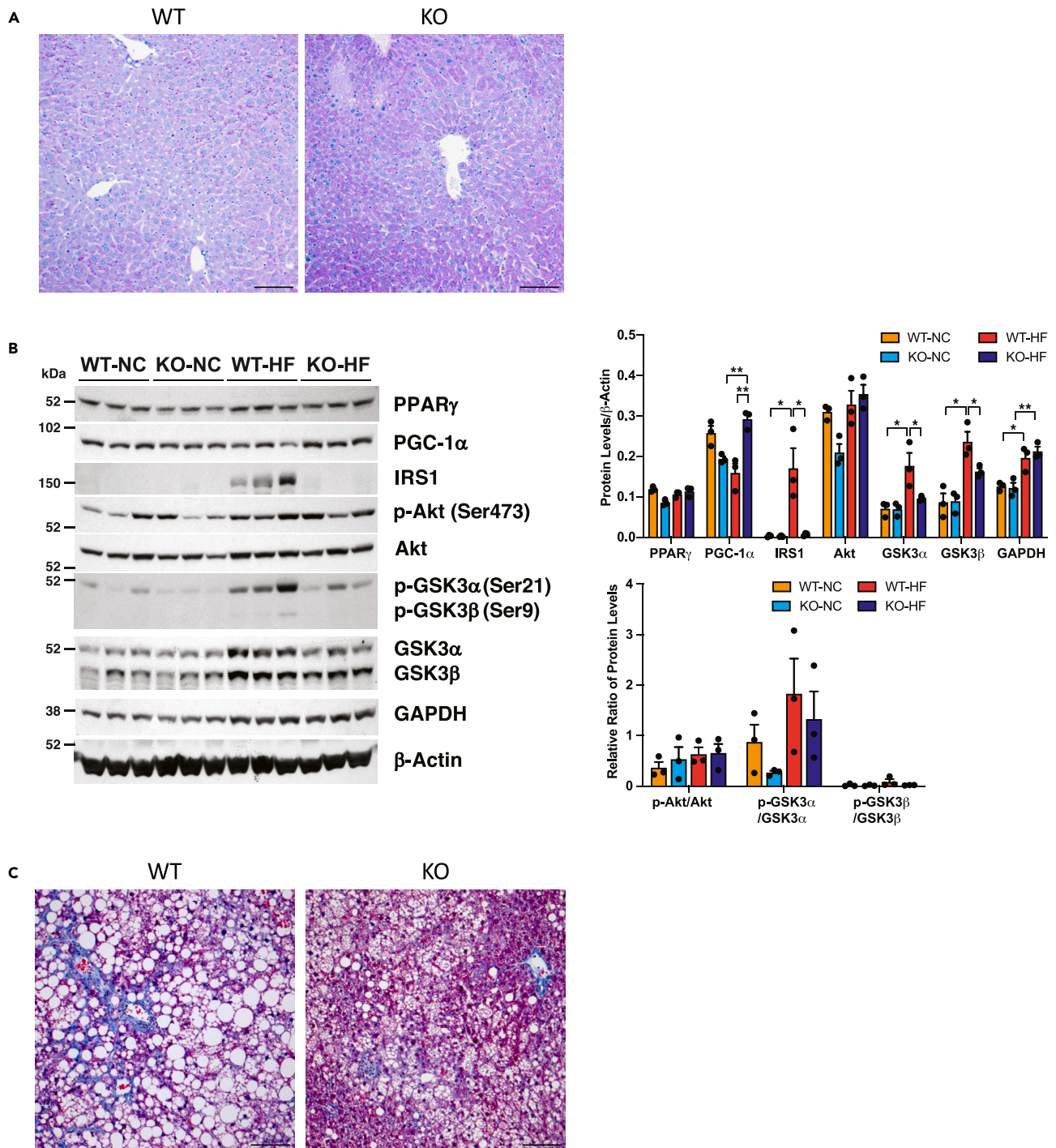
Figure 7. Increased glycogen content and decreased fibrosis in liver from the SKMiPLA$_2\gamma$KO mouse

(A) Glycogen present in hepatic tissue from WT and SKMiPLA$_2\gamma$KO mice fed a normal-chow diet was visualized by periodic acid-Shiff (PAS) staining with diastase digestion. The intensity of purple-magenta staining reflects the glycogen content of the hepatocytes in the representative histological images. Scale bar: 100 μm.

(B) Expression and phosphorylation levels of proteins involved in insulin signaling in livers from 3 WT to 3 SKMiPLA$_2\gamma$KO male mice fed either an NC or HF diet as determined by western blot analyses. Values are the means $\pm$ SEM. *$p < 0.05$ and **$p < 0.01$.

(C) Fibrosis in hepatic tissues from WT and SKMiPLA$_2\gamma$KO mice subjected to HF feeding was visualized by Masson's trichrome histopathological staining. Collagen fibers appear as filamentous blue structures in the representative histologic images. Scale bar: 100 μm.

obesity and heart failure.[26,27] Interestingly, the global absence of iPLA$_2\gamma$ in mice caused dramatic patho-logic abnormalities, which included diverse organ-dependent changes in mitochondrial ultrastructure, mitochondrial respiration, lipid content, and glucose tolerance/insulin sensitivity during high-fat feeding.[11] Recent work from our laboratory utilizing a hepatocyte-specific iPLA$_2\gamma$ KO mouse demonstrated resistance to an HF diet-facilitated Ca^{2+}-induced permeability transition in hepatic mitochondria and improved glucose clearance rates after HF feeding in comparison with WT controls.[17] In addition, genetic ablation of iPLA$_2\gamma$ demonstrated marked attenuation of non-oxidized and oxidized fatty acids in multiple disease states.[17,28–30] However, unlike the whole-body iPLA$_2\gamma$ KO mouse, the hepatocyte-specific iPLA$_2\gamma$ KO mouse did not display an inability to gain weight nor a reduction in neutral lipid accumulation, such as TAG in liver during HF feeding which were notable phenotypic characteristics of the germline iPLA$_2\gamma$ KO mouse. Intriguingly, in the current study, ablation of iPLA$_2\gamma$ in skeletal muscle prevented overall body-weight gain and detrimental TAG and/or DAG accumulation in liver and skeletal muscle with improved glucose tolerance with similar levels of blood insulin as WT controls following consumption of a HF diet. These results underscore the importance of skeletal muscle iPLA$_2\gamma$ loss of function in mediating inefficient skeletal muscle mitochondrial -bioenergetics, which is reflected in multiple metabolic networks mediating changes in the integration of organismal glucose and lipid metabolism.

Genetic ablation of skeletal muscle iPLA$_2\gamma$ affects whole-body energy homeostasis through skeletal muscle mitochondrial dysfunction which alters glucose and lipid metabolism during metabolic stress

Conventional screening for defects in glucose metabolism has traditionally employed GTT or ITT measure-ments after glucose or insulin challenge. These metrics have typically been utilized to assess the presence of diabetes and associated elements in the metabolic syndrome. Phenotypic characterization of the SKMiPLA$_2\gamma$KO mouse has highlighted the significance of mitochondrial iPLA$_2\gamma$ in skeletal muscle physi-ology and metabolism where increased glucose disposal rates are not reflected by an apparent increase in insulin signaling. Specifically, in the presence of mitochondrial dysfunction, as is present in the SKMiPLA$_2\gamma$KO mouse, the animal can employ multiple mechanisms to attempt to overcome its compro-mised bioenergetic status resulting from iPLA$_2\gamma$ loss of function. These include increased glucose extraction, which during mitochondrial dysfunction from metabolic stress (e.g., exercise) results in the processing of glucose to pyruvate/lactate but does not lead to the efficient production of cellular energy due to defects in skeletal mitochondrial respiration. Thus, conventional measures of glucose homeostasis may be misleading if the increase in glucose disposal rates exceeds the ability of mitochondria to process glycolytic end products into ATP or other high energy equivalents. Therefore, the seemingly salutary ef-fects of iPLA$_2\gamma$ on GTT results exhibited by the SKMiPLA$_2\gamma$KO are not indicative of bioenergetic benefit due to the underlying dysfunctional changes in mitochondria since iPLA$_2\gamma$ loss of function in mitochondria precludes the effective processing of the increased glucose extracted from serum. Further, the results demonstrate that additional metabolic pathways processing excessive glucose are employed in other or-gans, such as the generation of glycogen in the liver and the channeling of glucose-phosphate through the pentose phosphate shunt due to the defects in ETC respiratory chain function.

The profound alterations in mitochondrial respiration, morphology, membrane potential, and H$_2$O$_2$ generation demonstrate the severe dysfunctional status of mitochondria in the SKMiPLA$_2\gamma$KO mouse. Accordingly, the SKMiPLA$_2\gamma$KO mouse has limited metabolic flexibility and its adaptive biochemical changes are unable to metabolize glycolytic products during metabolic stress resulting in decreased me-chanical strength, exercise tolerance, muscle growth, and metabolic efficiency. Moreover, these alterations have profound effects on organismal bioenergetics since both liver and adipose tissue alterations are man-ifested despite the presence of functional iPLA$_2\gamma$ in these tissues. Thus, although the increased uptake of glucose from serum and increased insulin sensitivity by conventional criteria are present in the SKMiPLA$_2\gamma$KO mouse, they are in reality a result of the underlying metabolic dysfunction arising from the shunting of glucose away from glycolysis toward alternative metabolic fates.

Skeletal muscle iPLA$_2\gamma$ participates in the maintenance of mitochondrial cardiolipin homeostasis which regulates mitochondrial electron chain complex activities

Cardiolipin (CL) is a class of phospholipids, which is specifically present in mitochondria with a unique chemical structure comprising ~20% of total mitochondrial lipids. Association of CL with the inner mito-chondrial membrane has been implicated in its prominent role sustaining mitochondrial bioenergetics through affecting membrane-binding of cytochrome c, enzyme complexes of the TCA cycle, and those

catalyzing oxidative phosphorylation.[31,32] Previous studies have emphasized that the acyl-chain composition of negatively charged CL is correlated with the stability and coordinated functions of ETC complexes and mitochondrial GTPases.[20–22,33,34] Accumulating evidence has suggested that CL molecular species are critical in the interaction and assembly of respiratory supercomplex subunits present in the mitochondrial inner membrane and in the matrix.[35–38] It has been previously reported that complex I and II activities were highly affected by the molecular species composition of CL present in mitochondrial membranes.[39–41] Moreover, our laboratory reported that dramatic redistribution of C18:2 fatty acyl-containing CL to C22:6 fatty acyl-containing CL was present in both STZ-induced diabetic and ob/ob mouse myocardium.[42] Since polyunsaturated fatty acyl-CLs are highly susceptible to ROS-mediated oxidation, the increase in C22:6-containing CL during HF feeding may represent one of the causes of inefficient mitochondrial respiration in the obese state. Our previous studies reported that iPLA$_2\gamma$ is a regulator of CL remodeling in multiple tissues since germline ablation of iPLA$_2\gamma$ demonstrated alterations in CL content/molecular species composition, and the purified recombinant iPLA$_2\gamma$ enzyme efficiently hydrolyzed both CL and oxidized CL releasing (oxidized) monolyso-CL and (oxidized) fatty acids.[10,12,43] Interestingly, this study demonstrates that CL remodeling in the absence of skeletal muscle iPLA$_2\gamma$ resulted in significant alterations in the profile of CL molecular species including a reduction in C18:2 fatty acyl-containing CL regardless of diet type. The amounts of C22:6-containing CL present in the skeletal muscle of the SKMiPLA$_2\gamma$KO during HF feeding was significantly lower in comparison to equivalent WT controls. Thus, alterations in CL content mediated by the absence of skeletal muscle iPLA$_2\gamma$ likely destabilize the interactions of multi-protein respiratory complexes and GTPases resulting in their attenuated catalytic activities and resultant mitochondrial morphologic changes. Supporting this notion, the activities of electron transfer complexes I and II were dramatically attenuated in SKMiPLA$_2\gamma$KO skeletal muscle mitochondria. These results suggest that iPLA$_2\gamma$-mediated changes in lipid composition alter mitochondrial membrane dynamics and preclude subsequent efficient ETC complex formation.

Impaired mitochondrial fusion/fission in SKMiPLA$_2\gamma$KO skeletal muscle induces the formation of dysmorphic mitochondria, mitochondrial dysfunction, and muscle atrophy

Mitochondria present in TA muscle from SKMiPLA$_2\gamma$KO mice display abnormal ultrastructural morphologies that are likely due to changes in not only the composition of membrane lipids but also certain mitochondrial protein complexes of the ETC, which collectively lead to mitochondrial dysfunction and resultant muscle atrophy. Previous studies have indicated that iPLA$_2\gamma$ remodels the mitochondrial membrane bilayer through changes in membrane lipid composition through targeting peroxidized phospholipids to release oxidized lipid second messengers.[11,44] Interestingly, this study identifies significant deficiencies in multiple critical mitochondrial fusion/fission proteins (*i.e.*, OPA1-long form, MFN1, and DRP1) in the SKMiPLA$_2\gamma$KO mouse. Although previous studies have emphasized the roles of mitochondrial fusion/fission proteins in the regulation of muscle development/hypertrophy, mitochondrial dynamics, and mitochondrial metabolic homeostasis, the exact mechanism(s) of GTPase action for these processes are largely unknown.[45–48] Recently, Favaro et al. and Dulac et al. reported that deletion of muscle-specific DRP1 in mice displayed severe muscle wasting and weakness inducing muscle atrophy. Notably, the SKMiPLA$_2\gamma$KO mice described in this study share many similar characteristics with these muscle-specific DRP1 KO mice.[45,49] These include low body-weight gain with either an NC or HF diet, modified mitochondrial structure, an increased population of depolarized mitochondria with decreased respiratory capacity, myofibril degeneration and regeneration (indicated by centralized myofiber nuclei), and decreased ETC protein levels, leading to mitochondrial dysfunction and postnatal lethality. Furthermore, OPA1 present in the inner membrane of mitochondria has been reported as a critical regulator for cristae morphology, stability of electron chain complexes, and apoptotic cell death.[50–52] Thus, alteration in fusion/fission protein expression levels observed in the SKMiPLA$_2\gamma$KO mouse muscle likely contribute to the abnormal mitochondrial morphology through disrupted mitochondrial dynamics further exacerbating mitochondrial dysfunction.

Collectively, the present study demonstrates that iPLA$_2\gamma$ mediates skeletal muscle bioenergetic function through multiple mechanisms including: 1) the preservation of mitochondrial structural and functional integrity; 2) the appropriate membrane environment (*e.g.*, surface charge, assembly of protein complexes, mitochondrial membrane morphology for optimal mitochondria function; and 3) concerted signaling of skeletal muscle with the liver for inter-organ impedance matching to facilitate metabolic flexibility in organismal bioenergetics. These critical roles of skeletal muscle iPLA$_2\gamma$ are underscored by the clear presence of

a multicomponent myopathy that has pathophysiologic effects on skeletal muscle bioenergetics, mechanical function, and whole-body energy metabolism.

Limitations of the study

The results of the present study identify mitochondrial dysfunction by multiple orthogonal metrics. These include alterations in CL content and molecular species distribution, changes in respiratory function, and altered mitochondrial dynamics. The observed mitochondrial dysfunction is multifactorial in nature and it is not possible to identify a single precipitating cause. Nevertheless, the results clearly identify that the compromised bioenergetic and physiologic phenotype of the skeletal muscle iPLA$_2$γ KO mouse is due to mitochondrial dysfunction. Further, *ex vivo* isometric maximal muscle force measurements revealed no significant differences in specific peak tetanic tensions after normalization to muscle PCSA between WT vs. SKMiPLA$_2$γKO mice. Since skeletal muscle uses mainly glucose for energy production during short-term exercise, this method likely has limitations for evaluating overall muscle function with underlying mitochondrial OXPHOS activity. However, since no difference in specific force was observed, we cannot exclude the possibility of neurological and/or behavioral defects in the SKMiPLA$_2$γKO mouse contributing to muscle weakness and atrophy.

STAR★METHODS

Detailed methods are provided in the online version of this paper and include the following:

- KEY RESOURCES TABLE
- RESOURCE AVAILABILITY
  - Lead contact
  - Materials availability
  - Data and code availability
- EXPERIMENTAL MODEL AND SUBJECT DETAILS
  - Generation of skeletal muscle-specific iPLA$_2$γ knockout mice
  - Animal diets and study protocols
- METHOD DETAILS
  - Skeletal muscle strength tests
  - High-resolution permeabilized tissue respirometry
  - Mitochondrial membrane potentiometry
  - Glucose and insulin tolerance tests
  - Lipidomics
  - EM for skeletal muscle tissue
  - Complex I activity assay
  - Complex II activity assay
  - Determination of mitochondrial reactive oxygen species production
  - Tissue staining and imaging
  - Ex-vivo maximal isometric tetanic force measurements
  - Quantitative RT-PCR (qRT-PCR)
  - Determination of mitochondrial DNA copy number
- QUANTIFICATION AND STATISTICAL ANALYSIS

SUPPLEMENTAL INFORMATION

Supplemental information can be found online at https://doi.org/10.1016/j.isci.2023.106895.

REFERENCES

1. Hood, D.A., Memme, J.M., Oliveira, A.N., and Triolo, M. (2019). Maintenance of skeletal muscle mitochondria in health, exercise, and aging. Annu. Rev. Physiol. *81*, 19–41. https://doi.org/10.1146/annurev-physiol-020518-114310.

2. Merz, K.E., and Thurmond, D.C. (2020). Role of skeletal muscle in insulin resistance and glucose uptake. Compr. Physiol. *10*, 785–809. https://doi.org/10.1002/cphy.c190029.

3. Gancheva, S., Jelenik, T., Álvarez-Hernández, E., and Roden, M. (2018). Interorgan metabolic crosstalk in human insulin resistance. Physiol. Rev. *98*, 1371–1415. https://doi.org/10.1152/physrev.00015.2017.

4. Priest, C., and Tontonoz, P. (2019). Inter-organ cross-talk in metabolic syndrome. Nat. Metab. *1*, 1177–1188. https://doi.org/10.1038/s42255-019-0145-5.

5. Severinsen, M.C.K., and Pedersen, B.K. (2020). Muscle-organ Crosstalk: the emerging roles of myokines. Endocr. Rev. *41*, 594–609. https://doi.org/10.1210/endrev/bnaa016.

6. Hajeyah, A.A., Griffiths, W.J., Wang, Y., Finch, A.J., and O'Donnell, V.B. (2020). The biosynthesis of enzymatically oxidized lipids. Front. Endocrinol. *11*, 591819. https://doi.org/10.3389/fendo.2020.591819.

7. Tourdot, B.E., Ahmed, I., and Holinstat, M. (2014). The emerging role of oxylipins in thrombosis and diabetes. Front. Pharmacol. *4*, 176. https://doi.org/10.3389/fphar.2013.00176.

8. Ayilavarapu, S., Kantarci, A., Fredman, G., Turkoglu, O., Omori, K., Liu, H., Iwata, T., Yagi, M., Hasturk, H., and Van Dyke, T.E. (2010). Diabetes-induced oxidative stress is mediated by Ca2+-independent phospholipase A2 in neutrophils. J. Immunol. *184*, 1507–1515. https://doi.org/10.4049/jimmunol.0901219.

9. Nelson, A.J., Stephenson, D.J., Bone, R.N., Cardona, C.L., Park, M.A., Tusing, Y.G., Lei, X., Kokotos, G., Graves, C.L., Mathews, C.E., et al. (2020). Lipid mediators and biomarkers associated with type 1 diabetes development. JCI Insight *5*, e138034. https://doi.org/10.1172/jci.insight.138034.

10. Mancuso, D.J., Sims, H.F., Han, X., Jenkins, C.M., Guan, S.P., Yang, K., Moon, S.H., Pietka, T., Abumrad, N.A., Schlesinger, P.H., and Gross, R.W. (2007). Genetic ablation of calcium-independent phospholipase A2gamma leads to alterations in mitochondrial lipid metabolism and function resulting in a deficient mitochondrial bioenergetic phenotype. J. Biol. Chem. *282*, 34611–34622.

11. Mancuso, D.J., Sims, H.F., Yang, K., Kiebish, M.A., Su, X., Jenkins, C.M., Guan, S., Moon, S.H., Pietka, T., Nassir, F., et al. (2010). Genetic ablation of calcium-independent phospholipase A2gamma prevents obesity and insulin resistance during high fat feeding by mitochondrial uncoupling and increased adipocyte fatty acid oxidation. J. Biol. Chem. *285*, 36495–36510. https://doi.org/10.1074/jbc.M110.115766.

12. Mancuso, D.J., Kotzbauer, P., Wozniak, D.F., Sims, H.F., Jenkins, C.M., Guan, S., Han, X., Yang, K., Sun, G., Malik, I., et al. (2009). Genetic ablation of calcium-independent phospholipase A2gamma leads to alterations in hippocampal cardiolipin content and molecular species distribution, mitochondrial degeneration, autophagy, and cognitive dysfunction. J. Biol. Chem. *284*, 35632–35644.

13. Yoda, E., Hachisu, K., Taketomi, Y., Yoshida, K., Nakamura, M., Ikeda, K., Taguchi, R., Nakatani, Y., Kuwata, H., Murakami, M., et al. (2010). Mitochondrial dysfunction and reduced prostaglandin synthesis in skeletal muscle of Group VIB Ca2+-independent phospholipase A2gamma-deficient mice. J. Lipid Res. *51*, 3003–3015. https://doi.org/10.1194/jlr.M008060.

14. Saunders, C.J., Moon, S.H., Liu, X., Thiffault, I., Coffman, K., LePichon, J.B., Taboada, E., Smith, L.D., Farrow, E.G., Miller, N., et al. (2015). Loss of function variants in human PNPLA8 encoding calcium-independent phospholipase A2 gamma recapitulate the mitochondriopathy of the homologous null mouse. Hum. Mutat. *36*, 301–306. https://doi.org/10.1002/humu.22743.

15. Shukla, A., Saneto, R.P., Hebbar, M., Mirzaa, G., and Girisha, K.M. (2018). A neurodegenerative mitochondrial disease phenotype due to biallelic loss-of-function variants in PNPLA8 encoding calcium-independent phospholipase A2gamma. Am. J. Med. Genet. *176*, 1232–1237. https://doi.org/10.1002/ajmg.a.38687.

16. Mancuso, D.J., Jenkins, C.M., Sims, H.F., Cohen, J.M., Yang, J., and Gross, R.W. (2004). Complex transcriptional and translational regulation of iPLA2gamma resulting in multiple gene products containing dual competing sites for mitochondrial or peroxisomal localization. Eur. J. Biochem. *271*, 4709–4724.

17. Moon, S.H., Dilthey, B.G., Liu, X., Guan, S., Sims, H.F., and Gross, R.W. (2021). High-fat diet activates liver iPLA2gamma generating eicosanoids that mediate metabolic stress. J. Lipid Res. *62*, 100052. https://doi.org/10.1016/j.jlr.2021.100052.

18. Li, H., and Sartorelli, V. (2018). ATP citrate lyase: a new player linking skeletal muscle metabolism and Epigenetics. Trends Endocrinol. Metab. *29*, 202–204. https://doi.org/10.1016/j.tem.2018.01.006.

19. Das, S., Morvan, F., Morozzi, G., Jourde, B., Minetti, G.C., Kahle, P., Rivet, H., Brebbia, P., Toussaint, G., Glass, D.J., and Fornaro, M. (2017). ATP citrate lyase regulates myofiber differentiation and increases regeneration by altering histone acetylation. Cell Rep. *21*, 3003–3011. https://doi.org/10.1016/j.celrep.2017.11.038.

20. Robinson, N.C. (1993). Functional binding of cardiolipin to cytochrome c oxidase. J. Bioenerg. Biomembr. 25, 153–163.

21. Zhang, M., Mileykovskaya, E., and Dowhan, W. (2002). Gluing the respiratory chain together. Cardiolipin is required for supercomplex formation in the inner mitochondrial membrane. J. Biol. Chem. 277, 43553–43556.

22. Pfeiffer, K., Gohil, V., Stuart, R.A., Hunte, C., Brandt, U., Greenberg, M.L., and Schägger, H. (2003). Cardiolipin stabilizes respiratory chain supercomplexes. J. Biol. Chem. 278, 52873–52880.

23. DeFronzo, R.A., and Tripathy, D. (2009). Skeletal muscle insulin resistance is the primary defect in type 2 diabetes. Diabetes Care 32, S157–S163.

24. Sylow, L., Tokarz, V.L., Richter, E.A., and Klip, A. (2021). The many actions of insulin in skeletal muscle, the paramount tissue determining glycemia. Cell Metab. 33, 758–780. https://doi.org/10.1016/j.cmet.2021.03.020.

25. Sartori, R., Romanello, V., and Sandri, M. (2021). Mechanisms of muscle atrophy and hypertrophy: implications in health and disease. Nat. Commun. 12, 330. https://doi.org/10.1038/s41467-020-20123-1.

26. Prunonosa Cervera, I., Gabriel, B.M., Aldiss, P., and Morton, N.M. (2021). The phospholipase A2 family's role in metabolic diseases: focus on skeletal muscle. Physiol. Rep. 9, e14662. https://doi.org/10.14814/phy2.14662.

27. Moon, S.H., Liu, X., Cedars, A.M., Yang, K., Kiebish, M.A., Joseph, S.M., Kelley, J., Jenkins, C.M., and Gross, R.W. (2018). Heart failure-induced activation of phospholipase iPLA2gamma generates hydroxyeicosatetraenoic acids opening the mitochondrial permeability transition pore. J. Biol. Chem. 293, 115–129. https://doi.org/10.1074/jbc.RA117.000405.

28. Moon, S.H., Mancuso, D.J., Sims, H.F., Liu, X., Nguyen, A.L., Yang, K., Guan, S., Dilthey, B.G., Jenkins, C.M., Weinheimer, C.J., et al. (2016). Cardiac myocyte-specific Knock-out of calcium-independent phospholipase A2gamma (iPLA2gamma) decreases oxidized fatty acids during Ischemia/Reperfusion and reduces Infarct size. J. Biol. Chem. 291, 19687–19700. https://doi.org/10.1074/jbc.M116.740597.

29. Moon, S.H., Jenkins, C.M., Liu, X., Guan, S., Mancuso, D.J., and Gross, R.W. (2012). Activation of mitochondrial calcium-independent phospholipase A2gamma (iPLA2gamma) by divalent cations mediating arachidonate release and production of downstream eicosanoids. J. Biol. Chem. 287, 14880–14895. https://doi.org/10.1074/jbc.M111.336776.

30. Liu, X., Moon, S.H., Mancuso, D.J., Jenkins, C.M., Guan, S., Sims, H.F., and Gross, R.W. (2013). Oxidized fatty acid analysis by charge-switch derivatization, selected reaction monitoring, and accurate mass quantitation.

Anal. Biochem. 442, 40–50. https://doi.org/10.1016/j.ab.2013.06.014.

31. Fox, C.A., and Ryan, R.O. (2022). Studies of the cardiolipin interactome. Prog. Lipid Res. 88, 101195. https://doi.org/10.1016/j.plipres.2022.101195.

32. Gasanoff, E.S., Yaguzhinsky, L.S., and Garab, G. (2021). Cardiolipin, non-bilayer structures and mitochondrial bioenergetics: relevance to cardiovascular disease. Cells 10. https://doi.org/10.3390/cells10071721.

33. Ban, T., Heymann, J.A.W., Song, Z., Hinshaw, J.E., and Chan, D.C. (2010). OPA1 disease alleles causing dominant optic atrophy have defects in cardiolipin-stimulated GTP hydrolysis and membrane tubulation. Hum. Mol. Genet. 19, 2113–2122. https://doi.org/10.1093/hmg/ddq088.

34. Bustillo-Zabalbeitia, I., Montessuit, S., Raemy, E., Basañez, G., Terrones, O., and Martinou, J.C. (2014). Specific interaction with cardiolipin triggers functional activation of Dynamin-Related Protein 1. PLoS One 9, e102738. https://doi.org/10.1371/journal.pone.0102738.

35. Fiedorczuk, K., Letts, J.A., Degliesposti, G., Kaszuba, K., Skehel, M., and Sazanov, L.A. (2016). Atomic structure of the entire mammalian mitochondrial complex I. Nature 538, 406–410. https://doi.org/10.1038/nature19794.

36. Gonzalvez, F., D'Aurelio, M., Boutant, M., Moustapha, A., Puech, J.P., Landes, T., Arnauné-Pelloquin, L., Vial, G., Taleux, N., Slomianny, C., et al. (2013). Barth syndrome: cellular compensation of mitochondrial dysfunction and apoptosis inhibition due to changes in cardiolipin remodeling linked to tafazzin (TAZ) gene mutation. Biochim. Biophys. Acta 1832, 1194–1206. https://doi.org/10.1016/j.bbadis.2013.03.005.

37. Dudek, J., Cheng, I.F., Balleininger, M., Vaz, F.M., Streckfuss-Bömeke, K., Hübscher, D., Vukotic, M., Wanders, R.J.A., Rehling, P., and Guan, K. (2013). Cardiolipin deficiency affects respiratory chain function and organization in an induced pluripotent stem cell model of Barth syndrome. Stem Cell Res. 11, 806–819. https://doi.org/10.1016/j.scr.2013.05.005.

38. Lange, C., Nett, J.H., Trumpower, B.L., and Hunte, C. (2001). Specific roles of protein-phospholipid interactions in the yeast cytochrome bc1 complex structure. EMBO J. 20, 6591–6600. https://doi.org/10.1093/emboj/20.23.6591.

39. Fry, M., and Green, D.E. (1981). Cardiolipin requirement for electron transfer in complex I and III of the mitochondrial respiratory chain. J. Biol. Chem. 256, 1874–1880.

40. Schwall, C.T., Greenwood, V.L., and Alder, N.N. (2012). The stability and activity of respiratory Complex II is cardiolipin-dependent. Biochim. Biophys. Acta 1817, 1588–1596. https://doi.org/10.1016/j.bbabio.2012.04.015.

41. Paradies, G., Petrosillo, G., Pistolese, M., and Ruggiero, F.M. (2002). Reactive oxygen species affect mitochondrial electron

transport complex I activity through oxidative cardiolipin damage. Gene 286, 135–141. https://doi.org/10.1016/s0378-1119(01)00814-9.

42. Han, X., Yang, J., Yang, K., Zhao, Z., Abendschein, D.R., and Gross, R.W. (2007). Alterations in myocardial cardiolipin content and composition occur at the very earliest stages of diabetes: a shotgun lipidomics study. Biochemistry 46, 6417–6428. https://doi.org/10.1021/bi7004015.

43. Liu, G.Y., Moon, S.H., Jenkins, C.M., Li, M., Sims, H.F., Guan, S., and Gross, R.W. (2017). The phospholipase iPLA2gamma is a major mediator releasing oxidized aliphatic chains from cardiolipin, integrating mitochondrial bioenergetics and signaling. J. Biol. Chem. 292, 10672–10684. https://doi.org/10.1074/jbc.M117.783068.

44. Jaburek, M., Pruchova, P., Holendova, B., Galkin, A., and Jezek, P. (2021). Antioxidant synergy of mitochondrial phospholipase PNPLA8/iPLA2gamma with fatty acid-conducting SLC25 gene family transporters. Antioxidants 10. https://doi.org/10.3390/antiox10050678.

45. Dulac, M., Leduc-Gaudet, J.P., Reynaud, O., Ayoub, M.B., Guérin, A., Finkelchtein, M., Hussain, S.N., and Gouspillou, G. (2020). Drp1 knockdown induces severe muscle atrophy and remodelling, mitochondrial dysfunction, autophagy impairment and denervation. J. Physiol. 598, 3691–3710. https://doi.org/10.1113/JP279802.

46. Gandhi, S., and Perry, C.G.R. (2020). Mapping the role of mitochondrial DRP1 in skeletal muscle health: is too much and too little a bad thing? J. Physiol. 598, 3539–3540. https://doi.org/10.1113/JP280316.

47. Tezze, C., Romanello, V., Desbats, M.A., Fadini, G.P., Albiero, M., Favaro, G., Ciciliot, S., Soriano, M.E., Morbidoni, V., Cerqua, C., et al. (2017). Age-associated loss of OPA1 in muscle impacts muscle mass, metabolic homeostasis, systemic Inflammation, and Epithelial Senescence. Cell Metab. 25, 1374–1389.e6. https://doi.org/10.1016/j.cmet.2017.04.021.

48. Chen, H., Detmer, S.A., Ewald, A.J., Griffin, E.E., Fraser, S.E., and Chan, D.C. (2003). Mitofusins Mfn1 and Mfn2 coordinately regulate mitochondrial fusion and are essential for embryonic development. J. Cell Biol. 160, 189–200. https://doi.org/10.1083/jcb.200211046.

49. Favaro, G., Romanello, V., Varanita, T., Andrea Desbats, M., Morbidoni, V., Tezze, C., Albiero, M., Canato, M., Gherardi, G., De Stefani, D., et al. (2019). DRP1-mediated mitochondrial shape controls calcium homeostasis and muscle mass. Nat. Commun. 10, 2576. https://doi.org/10.1038/s41467-019-10226-9.

50. Frezza, C., Cipolat, S., Martins de Brito, O., Micaroni, M., Beznoussenko, G.V., Rudka, T., Bartoli, D., Polishuck, R.S., Danial, N.N., De Strooper, B., and Scorrano, L. (2006). OPA1 controls apoptotic cristae remodeling independently from mitochondrial fusion.

Cell *126*, 177–189. https://doi.org/10.1016/j.cell.2006.06.025.

51. Cogliati, S., Frezza, C., Soriano, M.E., Varanita, T., Quintana-Cabrera, R., Corrado, M., Cipolat, S., Costa, V., Casarin, A., Gomes, L.C., et al. (2013). Mitochondrial cristae shape determines respiratory chain supercomplexes assembly and respiratory efficiency. Cell *155*, 160–171. https://doi.org/10.1016/j.cell.2013.08.032.

52. Ishihara, N., Fujita, Y., Oka, T., and Mihara, K. (2006). Regulation of mitochondrial morphology through proteolytic cleavage of OPA1. EMBO J. *25*, 2966–2977. https://doi.org/10.1038/sj.emboj.7601184.

53. Moon, S.H., Jenkins, C.M., Kiebish, M.A., Sims, H.F., Mancuso, D.J., and Gross, R.W. (2012). Genetic ablation of calcium-independent phospholipase A2gamma (iPLA2gamma) attenuates calcium-induced opening of the mitochondrial permeability transition pore and resultant cytochrome c release. J. Biol. Chem. *287*, 29837–29850. https://doi.org/10.1074/jbc.M112.373654.

54. Han, X., Yang, J., Cheng, H., Yang, K., Abendschein, D.R., and Gross, R.W. (2005). Shotgun lipidomics identifies cardiolipin depletion in diabetic Myocardium Linking altered substrate utilization with mitochondrial dysfunction. Biochemistry *44*, 16684–16694.

55. Han, X., Yang, K., Yang, J., Cheng, H., and Gross, R.W. (2006). Shotgun lipidomics of cardiolipin molecular species in lipid extracts of biological samples. J. Lipid Res. *47*, 864–879. https://doi.org/10.1194/jlr.D500044-JLR200.

56. Wang, M., Hayakawa, J., Yang, K., and Han, X. (2014). Characterization and quantification of diacylglycerol species in biological extracts after one-step derivatization: a shotgun lipidomics approach. Anal. Chem. *86*, 2146–2155. https://doi.org/10.1021/ac403798q.

57. Bengoechea, R., Pittman, S.K., Tuck, E.P., True, H.L., and Weihl, C.C. (2015). Myofibrillar disruption and RNA-binding protein aggregation in a mouse model of limb-girdle muscular dystrophy 1D. Hum. Mol. Genet. *24*, 6588–6602. https://doi.org/10.1093/hmg/ddv363.

58. Biltz, N.K., Collins, K.H., Shen, K.C., Schwartz, K., Harris, C.A., and Meyer, G.A. (2020). Infiltration of intramuscular adipose tissue impairs skeletal muscle contraction. J. Physiol. *598*, 2669–2683. https://doi.org/10.1113/JP279595.

59. Quiros, P.M., Goyal, A., Jha, P., and Auwerx, J. (2017). Analysis of mtDNA/nDNA ratio in mice. Curr. Protoc. Mouse Biol. *7*, 47–54. https://doi.org/10.1002/cpmo.21.

STAR★METHODS

KEY RESOURCES TABLE

REAGENT or RESOURCE	SOURCE	IDENTIFIER
Antibodies		
COX IV (D6I4K) Rabbit mAb (Rodent Specific) antibody	Cell Signaling Technology	Cat# 38563; RRID:AB_2799136
DRP1 (D8H5) Rabbit mAb antibody	Cell Signaling Technology	Cat# 5391; RRID:AB_11178938
VDAC (D73D12) Rabbit mAb antibody	Cell Signaling Technology	Cat# 4661; RRID:AB_10557420
OPA1 (D6U6N) Rabbit mAb antibody	Cell Signaling Technology	Cat# 80471; RRID:AB_2734117
SQSTM1/p62 Antibody	Cell Signaling Technology	Cat# 5114; RRID:AB_10624872
Citrate Synthase (D7V8B) Rabbit mAb antibody	Cell Signaling Technology	Cat# 14309; RRID:AB_2665545
Mitofusin-2 (D2D10) Rabbit mAb antibody	Cell Signaling Technology	Cat# 9482; RRID:AB_2716838
β-Actin (8H10D10) Mouse mAb antibody	Cell Signaling Technology	Cat# 3700; RRID:AB_2242334
Akt Antibody	Cell Signaling Technology	Cat# 9272; RRID:AB_329827
Phospho-Akt (Ser473) (D9E) XP® Rabbit mAb antibody	Cell Signaling Technology	Cat# 4060; RRID:AB_2315049
LC3B antibody	Cell Signaling Technology	Cat# 2775; RRID:AB_915950
SDHA (D6J9M) XP antibody	Cell Signaling Technology	Cat# 11998; RRID:AB_2750900
IRS-1 (59G8) Rabbit mAb antibody	Cell Signaling Technology	Cat# 2390; RRID:AB_10692516
GSK-3α/β (D75D3) Rabbit mAb antibody	Cell Signaling Technology	Cat# 5676; RRID:AB_10547140
Phospho-GSK-3α/β (Ser21/9) antibody	Cell Signaling Technology	Cat# 9331; RRID:AB_329830
S6 Ribosomal Protein (5G10) Rabbit mAb antibody	Cell Signaling Technology	Cat# 2217; RRID:AB_331355
Phospho-S6 Ribosomal Protein (Ser235/236) antibody	Cell Signaling Technology	Cat# 2211; RRID:AB_331679
Anti-rabbit IgG, HRP-linked antibody	Cell Signaling Technology	Cat# 7074; RRID:AB_2099233
ATP-Citrate Lyase antibody	Cell Signaling Technology	Cat# 4332; RRID:AB_2223744
Phospho-ATP-Citrate Lyase (Ser455) antibody	Cell Signaling Technology	Cat# 4331; RRID:AB_2257987
UQCRC1 Polyclonal antibody	Thermo Fisher Scientific	Cat# PA5-21394; RRID:AB_11152122
Goat anti-Mouse IgG Fc Secondary Antibody, HRP	Thermo Fisher Scientific	Cat# A16084; RRID:AB_2534758
PGC-1 alpha antibody	Novus Biologicals	Cat# NBP1-04676; RRID:AB_1522118
MyoD antibody	Novus Biologicals	Cat# NBP1-54153; RRID:AB_11015772
PPAR gamma/NR1C3 antibody	Novus Biologicals	Cat# NBP2-22106; RRID:Not Available
GAPDH antibody (FL-335)	Santa Cruz Biotechnology	Cat# sc-25778; RRID:AB_10167668
myogenin (F5D)	Santa Cruz Biotechnology	Cat# sc-12732; RRID:AB_627980
Anti-cytochrome c antibody (A-8)	Santa Cruz Biotechnology	Cat# sc-13156; RRID:AB_627385
Goat Anti-ANT Polyclonal antibody	Santa Cruz Biotechnology	Cat# sc-9299; RRID:AB_671086
Mouse anti-goat IgG-HRP	Santa Cruz Biotechnology	Cat# sc-2354; RRID:AB_628490
MFN1 Polyclonal antibody	Proteintech	Cat# 13798-1-AP; RRID:AB_2266318
Monoclonal Anti-Myosin (Skeletal, Slow) antibody produced in mouse	MilliporeSigma	Cat# M8421; RRID:AB_477248
Monoclonal Anti-Myosin (Skeletal, Fast) antibody produced in mouse	MilliporeSigma	Cat# M1570; RRID:AB_2147168
Rabbit polyclonal anti-mouse iPLA$_2$γ antibody	This paper	N/A
Chemicals, peptides, and recombinant proteins		
10-Acetyl-3,7-dihydroxyphenoxazine (Amplex Red)	Cayman Chemical	Cat#10010469, CAS: 119171-73-2
Peroxidase from Horseradish	MilliporeSigma	P8375, CAS: 9003-99-0

(Continued on next page)

Continued

REAGENT or RESOURCE	SOURCE	IDENTIFIER
Rotenone	Cayman Chemical	Cat#13995, CAS:83-79-4
2,6-Dichlorophenol-indophenol sodium salt dihydrate	Sigma-Aldrich	Cat#33125-5G-R, CAS: 620-45-1
Lactobionic acid	Sigma-Aldrich	Cat#61321, CAS: 96-82-2
Sucrose	Thermo Fisher Scientific	BP220-212, CAS: 57-50-1
PageRuler™ Plus Prestained Protein Ladder	Thermo Fisher Scientific	Cat#26619
Amersham ECL Full-Range Rainbow Molecular Weight Markers	Cytiva	Cat# RPN800E
Dextrose	Fisher Scientific	D16-1, CAS: 50-99-7
PicoLab Rodent Diet 20	LabDiet	Cat#5053
Humulin R U-100 insulin	Lily USA, LLC	NDC 0002-8215-17 (HI-213)
Adjusted calories diet (42% from fat)	Envigo	Cat#TD.88137
TRIHEPTADECENOIN	Nucheck Prep, Inc.	T-404, CAS: 1858264-39-7
DIMYRISTOLEIN	Nucheck Prep, Inc.	D-206, CAS: 372516-89-7
14:0 Cardiolipin (ammonium salt)	Avanti Polar Lipids	Cat#710332, CAS: 63988-20-5
FCCP	Cayman Chemical	Cat#15218, CAS: 370-86-5
L-(−)-Malic acid	MilliporeSigma	M1000, CAS: 97-67-6
Sodium pyruvate	MilliporeSigma	P2256, CAS: 113-24-6
L-Glutamic acid monosodium salt hydrate	MilliporeSigma	G1626, CAS: 142-47-2
Adenosine 5′-diphosphate monopotassium salt dihydrate	MilliporeSigma	A5285, CAS: 72696-48-1
Antimycin A from *Streptomyces* sp.	MilliporeSigma	A8674, CAS: 1397-94-0
Sodium succinate dibasic hexahydrate	MilliporeSigma	S2378, CAS: 6106-21-4
Bovine Serum Albumin	MilliporeSigma	A8806, CAS: 9048-46-8
Cytochrome c from equine heart	MilliporeSigma	C7752, CAS: 9007-43-6
(−)-Blebbistatin	MilliporeSigma	B0560, CAS: 856925-71-8
Saponin from quillaja bark	MilliporeSigma	S7900, CAS: 8047-15-2
Creatine	MilliporeSigma	C0780, CAS: 57-00-1
Taurine	MilliporeSigma	T0625, CAS: 107-35-7
2-Thenoyltrifluoroacetone	MilliporeSigma	T27006, CAS: 326-91-0
Potassium cyanide	MilliporeSigma	60178, CAS: 151-50-8
Decylubiquinone	MilliporeSigma	D7911, CAS: 55486-00-5
Tragacanth	MilliporeSigma	G1128, CAS: 9000-65-1
2-Methylbutane	MilliporeSigma	M32631, CAS: 78-78-4
HEPES	MilliporeSigma	H3375, CAS: 7365-45-9
β-Nicotinamide adenine dinucleotide, reduced disodium salt	MilliporeSigma	N9410, CAS: 606-68-8
Tetraphenylphosphonium chloride	MilliporeSigma	Cat#218790, CAS: 2001-45-8
Hydrogen peroxide	MilliporeSigma	Cat#95321, CAS: 7722-84-1
Critical commercial assays		
Ultra Sensitive Mouse Insulin ELISA Kit	Crystal Chem	Cat#90080
BCA Protein Assay Kit	Fisher Scientific	PI23225
Reliance One-Step Multiplex RT-qPCR Supermix	Bio-Rad	Cat#12010176
QIAamp DNA Mini Kit	Qiagen	Cat#51304
TRIzol™ Reagent	Thermo Fisher Scientific	Cat# 15596026

Continued

REAGENT or RESOURCE	SOURCE	IDENTIFIER
Reference gene assay: mouse Ppia	Integrated DNA Technologies	Mm.PT.39a.2.gs
PowerUp™ SYBR™ Green Master Mix	Thermo Fisher Scientific	Cat# A25742
Gene expression assay: mouse Dnm1l	Thermo Fisher Scientific	Mm01342903_m1
Gene expression assay: mouse Mfn1	Thermo Fisher Scientific	Mm00612599_m1
Gene expression assay: mouse Opa1	Thermo Fisher Scientific	Mm00453879_m1
Experimental models: Organisms/strains		
Mouse: B6.Cg-Tg(ACTA1-cre)79Jme/J	The Jackson Laboratory	Cat# 006149
Oligonucleotides		
ND1 forward: 5′-CTAGCAGAAACAAACCGGGC-3′	Integrated DNA Technologies, Inc.	N/A
ND1 reverse: 5′-CCGGCTGCGTATTCTACGTT-3′	Integrated DNA Technologies, Inc.	N/A
HK2 forward: 5′-GCCAGCCTCTCCTGATTTTAGTGT-3′	Integrated DNA Technologies, Inc.	N/A
HK2 reverse: 5′-GGGAACACAAAAGACCTCTTCTGG-3′	Integrated DNA Technologies, Inc.	N/A
Software and algorithms		
Prism 9, ver 9.5.0	GraphPad Software	https://www.graphpad.com/
ChipSoft 8.3.3	Advion Biosciences, Inc.	
Other		
Finnigan TSQ Quantum Ultra	Thermo Fisher Scientific	
QuantStudio 3 Real-Time PCR Systems	Thermo Fisher Scientific	

RESOURCE AVAILABILITY

Lead contact

Further information and requests for resources and reagents should be directed to and will be fulfilled by the lead contact, Richard W. Gross (rgross@wustl.edu).

Materials availability

Skeletal muscle-specific iPLA$_2$γ KO mice in this study were generated in our laboratory.

Skeletal muscle-specific iPLA$_2$γ KO mice and the rabbit polyclonal anti-mouse iPLA$_2$γ antibody used in this study are available on request with material/rodent transfer agreement.

Data and code availability

- All data reported in this paper will be shared by the lead contact upon reasonable request.

- No new code has been generated in this study.

- Any additional information required to reanalyze the data reported in this paper is available from the lead contact upon request.

EXPERIMENTAL MODEL AND SUBJECT DETAILS

Generation of skeletal muscle-specific iPLA$_2$γ knockout mice

To generate the skeletal muscle-specific iPLA$_2$γ KO mouse, exon 5 (encoding the iPLA$_2$γ active site) was flanked by *loxP* sites as described previously[28] and ablated by crossing with a transgenic mouse expressing Cre-recombinase driven by the human alpha-actin promoter (The Jackson Laboratory, Cat. # 006149). Skeletal muscle-specific deletion of iPLA$_2$γ was confirmed by western blot analysis of mitochondria isolated from multiple tissues (white adipose, liver and skeletal muscle) probed with a rabbit polyclonal antibody directed against iPLA$_2$γ that our laboratory generated.[53]

Animal diets and study protocols

Male mice (6–8 months old) were used for animal studies except where comparisons were made between male and female mice. Mice were maintained and used in strict accordance with the National Institutes of Health guidelines for humane treatment of animals. All protocols for use of animals in this study were reviewed and approved by the Institutional Animal Care and Use Committee of Washington University. Mice were fed daily with a normal-chow diet (LabDiet, Cat. #5053). For experiments with mice fed a high-fat diet, mice at the age of 3 months were fed a Western diet with 42% kcal from fat (Envigo, Cat. #TD.88137) for 12–14 weeks.

METHOD DETAILS

Skeletal muscle strength tests

Mice aged of 6–7 months fed either a normal-chow or high-fat diet for 3 months were utilized for measurement of skeletal muscle strength including a fore-limb strength test, a four-limb hanging test and a treadmill test.

The fore-limb strength test was performed by using the grip strength meter. Mice held from the tip of the tail were placed on the grid and extended until mice grasped the grid with two fore-limbs. The mice were then pulled back until they released their grip from the grid and the maximum grip strength exerted by the mice grabbing the grid was then recorded.

The four-limb hanging test was performed by using a wire grid system to determine the ability of mice to support their gravitational weight. The length of time for the mice to remain suspended on the grid before falling was recorded.

The treadmill test was performed using a Columbus Instruments Exer 3/6 Treadmill. The resting levels of glucose and lactate present in tail blood samples were measured 2–3 days before the treadmill test. Mice were put in a treadmill cage and allowed to adjust to the new environment for 3–5 min. Treadmill training started at a running speed of 10 m/min and the speed was gradually increased by 3 m/min every 3 minutes. The length of elapsed time before the mice fell back to the shock-pad and were not able to return to the treadmill was recorded. When mice repeatedly failed to maintain running on the treadmill, they were removed from the cage and glucose and lactate levels were immediately measured in tail blood samples. For the experiments of high intensity interval treadmill exercise, mice were forced to run on the treadmill at 18m/min for 4 min and then glucose and lactate levels present in tail blood samples were immediately measured.

High-resolution permeabilized tissue respirometry

The tibialis anterior (TA) muscle was harvested from euthanized WT and SKMiPLA$_2\gamma$KO mice, placed in ice-cold PBS and shredded into fibers under a microscope within 5 min. The shredded TA tissue was then placed in fresh ice-cold PBS containing 25 μg/mL saponin and incubated in a cold room for 30 min with gentle stirring. Saponin-permeabilized fibers were then briefly washed with PBS, transferred into Mitochondrial Respiration Buffer (MiR05: 0.5mM EGTA, 3mM MgCl$_2$, 60mM K-lactobionate, 20mM taurine, 10mM KH$_2$PO$_4$, 20mM HEPES (pH 7.1), 110mM sucrose, 0.1% fatty acid-free BSA) and incubated for 10 min on ice. After filling the Oroboros chambers with MiR05 buffer containing creatine (3mg/mL) and blebbistatin (10 μM), the permeabilized TA fibers were weighed and ~1 mg of tissue was placed into chambers at 37°C. MiR05 buffer in the chambers was supplemented with pure O$_2$ gas until the dissolved O$_2$ concentration reached ~400 μM. Tissue respiration was initiated by adding substrates including malate (5 mM), glutamate (10 mM), and pyruvate (5 mM). ADP (5 mM), succinate (10 mM), cytochrome c (10 μM), FCCP (1 μM) and rotenone (1 μM) were sequentially added and steady state oxygen consumption rates were measured following the stepwise addition of each reagent. Oxygen consumption rates were normalized to the weight of the tissue used for respirometry.

Mitochondrial membrane potentiometry

Mitochondria from mouse TA tissue were isolated by a differential centrifugation method. Measurements of mitochondrial membrane potential were performed as previously described.[28] Briefly, tibialis anterior tissue was placed in Mitochondria Isolation Buffer (MIB) containing 0.21M mannitol, 0.07M sucrose, 0.1mM K-EDTA, 10mM Tris-HCl, 1mM EGTA, 0.5% BSA, pH 7.4 and cut into small pieces in a Petri dish

on ice. The pieces were transferred to a 10 mL Potter Elvehjem tissue grinder and homogenized using a rotorized homogenizer with a Teflon pestle for 12 strokes at 120 rpm. The homogenates were centrifuged at $850 \times g$ and the supernatant was collected. The supernatant was then centrifuged at $10,000 \times g$ and the mitochondrial pellet was resuspended in MIB without BSA. Mitochondrial membrane potential ($\Delta\Psi_{mt}$) measurements were performed using an Oroboros® Oxygraph 2K instrument equipped with a TPP^+ (tetraphenylphosphonium) ion selective electrode. Internal calibration of the membrane potential electrode using TPP·Cl standards (0.5, 1, 1.5, 2 µM) was performed before addition of 250 µg mitochondria into the MiR05 respiration buffer containing TPP·Cl (2 µM final concentration). Glutamate (10 mM)/pyruvate (5 mM)/malate (5 mM) (G P M) or succinate (Succ) (5 mM) were used as substrates for mitochondrial membrane potentiometry. The mitochondrial membrane potential was calculated according to the instructions provided by the manufacturer (OROBOROS INSTRUMENTS Corp).

Glucose and insulin tolerance tests

WT and SKMiPLA$_2\gamma$KO male mice (6-7 months old) fed with either a normal-chow or high-fat diet for 3 months were utilized for glucose and insulin tolerance tests. Mice were fasted for 16-18 hrs in cages without bedding but with free access to water prior to glucose tolerance tests. Glucose tolerance tests were initiated by the intraperitoneal injection of glucose (2 mg/g body weight). Blood was then drawn from the tail vein before (t=0 min) and at 15, 30, 60, 90 and 120 min after glucose administration. For insulin tolerance tests, mice were fasted for 4 hrs in cages prior to receiving an intraperitoneal injection of insulin (Humulin R U-100) (LillyUSA, LLC) at a dose of 0.75 units/kg body weight. Blood glucose levels were measured from blood drawn from the tail vein at 0, 15, 30, 60, 90 and 120 min after insulin injection. Glucose levels were measured using a Glucometer Elite (Bayer Corp., Elkhart, IN) and a Glucose Analyzer (Analox GM7 Analyser, Analox Instruments Inc., Lunenberg, MA). Lactate levels in blood were measured using a Lactate Plus meter (Nova Biomedical, MA).

Lipidomics

Lipid analyses were performed essentially as described previously.[11,54–56] In brief, neutral lipid extracts were initially extracted with 75% methanol and methyl-tert-butyl ether (MTBE), flushed with nitrogen, and re-extracted with hexane/methanol/water (1:1:0.1, v/v/v). The hexane layer was collected, dried, and stored at −20 °C prior to electrospray ionization-MS. A TSQ Quantum Ultra Plus triple-quadrupole mass spectrometer (Thermo Fisher Scientific, San Jose, CA) equipped with an automated nanospray apparatus (i.e., Nanomate HD, Advion Bioscience Ltd., Ithaca, NY) and Xcalibur system software was utilized. For DAG analysis, aliquots of the extracts from the hexane extraction were transferred to a glass tube and dried under a nitrogen stream. DAGs in the extracts were derivatized with N,N-dimethylglycine (DMG), extracted by Bligh-Dyer procedure, and quantitated by ESI-MS/MS using neutral loss scan of DMG (103 Da) as described previously.[56] For cardiolipin (CL) analysis, enhanced shotgun lipidomic analyses of cardiolipin (CL) were performed with a mass resolution setting of 0.3 Thomson by using extracts from the initial MTBE extraction of tissue as described previously in detail.[54,55] MS analysis employed, ionization voltages of 1.2 kV for DAG and TAG and 1.1 kV for CL, and gas pressure of 0.3 p.s.i. under control of ChipSoft 8.3.3 software. Each lipid extract solution was diluted with $CHCl_3/CH_3OH$/isopropyl alcohol (1:2:4, v/v/v) for TAG and DAG analyses or isopropyl alcohol for CL analysis prior to infusion into the mass spectrometer using the Nanomate apparatus.

EM for skeletal muscle tissue

Electron microscopic analyses of skeletal muscle were performed by the Center for Cellular Imaging at Washington University (WUCCI). Briefly, mice were euthanized by cervical dislocation and biopsy specimens from the tibialis anterior (TA) and quadricep (Quad) muscles were fixed in 2.5% glutaraldehyde + 2% paraformaldehyde (fresh, EM grade) in 0.15M cacodylate buffer with 2mM $CaCl_2$ (final concentrations) overnight at room temperature prior to storage at 4°C. Longitudinally sectioned skeletal muscle explants were then extensively washed in cacodylate buffer, post-fixed for 1 hr in OsO_4, rinsed with cacodylate buffer, then washed 3 times in H_2O, en bloc stained 1 hr in 1% uranyl acetate, dehydrated through a graded ethanol series to 100% propylene oxide and embedded in Araldite resin. Processed muscle tissue samples were then examined using a JEOL JEM-1400 120kV TEM instrument.

Complex I activity assay

Isolated mitochondria were placed in Mitochondria Isolation Buffer (MIB) without BSA and their membranes were disrupted by five freeze (in liquid N_2)-thaw (at room temperature) cycles. Mitochondria

were then placed in a 96 well-plate (5 µg mitochondrial protein/well) with MIB containing 150 µM decylubiquinone substrate, 2 mM KCN, 5 µM Antimycin A and 80 µM of the terminal electron acceptor, 2,6-dichlorophenolindophenol (DCIP). The Complex I NADH-ubiquinone reductase reaction was initiated by addition of NADH (160 µM final concentration) in the presence or absence of 5 µM rotenone. Complex I activity was monitored by measuring the absorbance decrease at 620 nm at 25 s intervals for 10 min at 37°C. The V_{max} of Complex I activity was determined from the initial linear time range of the absorbance decrease during the 10 min incubation. Experiments were performed for 5 independent preparations from each WT and SKMiPLA$_2$γKO groups of mice.

Complex II activity assay

Isolated mitochondria were placed in Mitochondria Isolation Buffer (MIB) without BSA and their membranes were disrupted by five freeze (in liquid N_2)-thaw (at room temperature) cycles. Mitochondria were then placed in a 96 well-plate (10 µg mitochondrial protein /well) with MIB containing 150 µM decylubiquinone substrate, 2 mM KCN, 5 µM antimycin A, 2 µM rotenone, and 80 µM of the terminal electron acceptor DCIP. The Complex II reaction was initiated by adding succinate substrate (20 mM final concentration) in the presence or absence of the Complex II inhibitor 2-thenoyltrifluoroacetone (TTFA, 0.5mM). Complex II activity was monitored by measuring the absorbance decrease at 620 nm with 25 s intervals for 10 min at 37°C. Complex II V_{max} was determined from the initial linear time range of the absorbance decrease during the 10 min incubation. Experiments were performed for 5 independent preparations from each WT and SKMiPLA$_2$γKO groups of mice.

Determination of mitochondrial reactive oxygen species production

The production of mitochondrial reactive oxygen species was monitored by utilizing Amplex Red (10-Acetyl-3,7-dihydroxyphenoxazine) to capture the hydrogen peroxide generated from forward and reverse electron transport. Briefly, mitochondria (10 µg protein) isolated from WT and SKMiPLA$_2$γKO mouse TA muscle were placed in wells of an opaque white 96-well microplate containing the assay buffer (20 mM HEPES (pH 7.2), 120 mM KCl, 1 mM $MgCl_2$, 2 mM KH_2PO_4, 0.1mM EDTA, 2.5 µM Amplex Red, 0.5 U/mL HRP and 0.025 % fatty acid-free BSA) at room temperature. For H_2O_2 production due to forward electron transport, glutamate (10 mM), pyruvate (5 mM) and malate (5 mM) were utilized as substrates in the presence or absence of 1 µM rotenone. For reverse electron transport, succinate (5 mM) was utilized as substrate in the presence or absence of 1 µM rotenone. No substrate was added to mitochondria as controls. The fluorescence of Amplex Red using 560 nm excitation and 590 nm emission wavelengths was measured after 5 min incubation at room temperature. The rate of H_2O_2 production was determined from a calibration curve of 0, 0.25, 0.5, 0.75, 1, 2.5, and 5 µM H_2O_2 standards.

Tissue staining and imaging

Hematoxylin and eosin (H & E) staining, Periodic Acid-Shiff (PAS) staining with diastase digestion and Masson's trichrome histopathological staining of liver tissue were performed by the Anatomic and Molecular Pathology Core Labs in Washington University. The image analyses of stained liver tissue were performed by the Center for Cellular Imaging at Washington University (WUCCI). Hematoxylin and eosin staining of skeletal muscle tissue was performed as described previously.[57] Briefly, tibialis anterior and quadriceps muscle tissues were mounted using tragacanth gum and frozen quickly in 2-methylbutane which was cooled in liquid nitrogen. The frozen tissue samples were sectioned at 10µm thickness, stained with hematoxylin & eosin on a coverslip, and photographed under a microscope.

Ex-vivo maximal isometric tetanic force measurements

Isometric muscle force measurements were performed as described previously.[58] Briefly, mice were continuously anesthetized with 2 % inhaled isoflurane at 2 L/min during dissection to maintain the viability of all muscles. The 5th toe muscle of the extensor digitorum longus (EDL) was dissected from one hindlimb. The EDL muscle was mounted in a specialized muscle physiology chamber (1300A, Aurora Scientific, ON, Canada) containing Ringers solution (137 mM NaCl, 5 mM KCl, 2 mM $CaCl_2$, 1 mM $MgSO_4$, 1 mM NaH_2PO_4, 24 mM $NaHCO_3$, 11 mM glucose with 10 mg/L curare) at 37°C. Insertion tendons were secured at the musculotendinous junction via an 8-0 suture to the arm of a dual mode ergometer (model 300B; Aurora Scientific, ON, Canada) while the tendon of origin was similarly secured to a rigid post. Muscle activation was provided by parallel plate electrodes flanking the muscle. Optimal muscle length was determined as the length at which supramaximal stimulation produces maximal isometric tetanic force. At optimal length,

force was recorded from an isometric twitch contraction, followed by an isometric tetanic contraction (300-ms train duration and 0.3 ms pulse duration at 225 Hz). Following each test, fiber length was measured through a dissecting microscope with an eyepiece micrometer scale reticule after which the muscle was cut free and weighed. All forces were normalized to the muscle physiological cross-sectional area (PCSA) with muscle density estimated at 1.056 g/cm^3.

Quantitative RT-PCR (qRT-PCR)

mRNA levels of genes in tibialis anterior from WT and SKMiPLA$_2$γKO mice were determined by quantitative real-time PCR, which was performed by the Genome Engineering and Stem Cell Center (GESC) at Washington University. Briefly, total RNA was extracted from TA tissues using TRIzol™ Reagent (Thermo Fisher Scientific). Quantitative RT-PCR was performed as one-step using Reliance One-Step Multiplex RT-qPCR Supermix (Bio-Rad) on QuantStudio™ 3 Real-Time PCR System according to manufacturer's instructions. The commercially available primers for the following mouse genes were purchased from Thermo Fisher Scientific: Drp1 (aka Dnm1l), Mm01342903_m1; Mfn1, Mm00612599_m1; and Opa1, Mm00453879_m1. Tissue mRNA levels were normalized to the level of an internal reference gene (mouse Ppia) in the same tissue sample. Relative gene expression levels were calculated using the $2^{-\Delta\Delta Ct}$ method.

Determination of mitochondrial DNA copy number

Mouse mitochondrial DNA copy numbers in TA muscle from WT and SKMiPLA$_2$γKO mice were determined by comparing ND1 mitochondrial-specific DNA expression relative to nuclear-specific Hexokinase 2 (HK2) DNA expression as previously described.[59] The number of copies of mtDNA was calculated using the following formula[59]:

$$\text{Copies of mtDNA} = 2 \times 2^{\Delta Ct},$$

where $\Delta Ct = Ct(\text{nDNA gene}) - Ct(\text{mtDNA gene})$.

QIAamp DNA Mini kit and PowerUp™ SYBR™ Green Master Mix were utilized for DNA isolation and qPCR assays, respectively. Primer sequences are as follows:

ND1, forward: 5'-CTAGCAGAAACAAACCGGGC-3', reverse: 5'-CCGGCTGCGTATTCTACGTT-3'; HK2, forward: 5'-GCCAGCCTCTCCTGATTTTAGTGT-3', reverse: 5'-GGGAACACAAAAGACCTCTTCTGG-3'.

QUANTIFICATION AND STATISTICAL ANALYSIS

A two-tailed Student *t* test was routinely performed to determine the significance of differences between two groups. A p-value < 0.05 was considered significant. All data are reported as the mean ± SEM. Statistical analysis was performed in GraphPad Prism 9.